INL/JOU-21-61613-Revision-0

Separate Effect Tests for Studying Temperature Gradient Driven Cracking in UO2 Pellets

July 2021

Sobhan Patnaik, Benjamin W Spencer, Elwyn Roberts, Theodore M. Besmann, Travis W. Knight

Changing the World's Energy Future

INL is a U.S. Department of Energy National Laboratory operated by Battelle Energy Alliance, LLC

INL/JOU-21-61613-Revision-0

Separate Effect Tests for Studying Temperature Gradient Driven Cracking in UO2 Pellets

Sobhan Patnaik, Benjamin W Spencer, Elwyn Roberts, Theodore M. Besmann, Travis W. Knight

July 2021

Idaho National Laboratory
Idaho Falls, Idaho 83415

http://www.inl.gov

Prepared for the
U.S. Department of Energy
Under DOE Idaho Operations Office
Contract DE-AC07-05ID14517

Separate Effects Tests for Studying Temperature-Gradient-Driven Cracking in UO_2 Pellets

S. Patnaik[1], B. W. Spencer[2], E. Roberts[1], T. M. Besmann[1], T. W. Knight[1]

[1] *University of South Carolina, Columbia, SC, USA*

[2] *Idaho National Laboratory, Idaho Falls, ID, USA*

Mailing Address:

Sobhan Patnaik

300 Main St., A224

Dept of Mechanical Engineering, University of South Carolina,

Columbia SC 29208

Email: spatnaik@email.sc.edu, Phone: +1208-206-7415

This paper is published as: S. Patnaik, B. W. Spencer, E. Roberts, T. M. Besmann, and T. W. Knight. Separate effects tests for studying temperature-gradient-driven cracking in UO2 pellets. Nuclear Science and Engineering, 195(12):1307–1326, 2021, doi: 10.1080/00295639.2021.1932223

Abstract

A variety of normal operation and accident scenarios can generate thermal stresses large enough to cause cracking in ceramic fuel pellets. Cracking in fuel pellets can lead to reduced heat removal, higher centerline temperatures, and localized stress in the cladding—all which impact fuel performance. It is important to experimentally characterize the thermal and mechanical behaviors in the pellet both before and after cracking which would help to improve cracking models in fuel performance codes such as BISON. However, in-reactor observation and measurement of cracking is very challenging due to the harsh environment and design of fuel rods involved. Recently, an experimental pellet-cracking test stand was developed for separate effects testing of pellet cracking under normal operations and accident temperature conditions, using thermal imaging to capture the pellet surface temperatures in order to evaluate the thermal stresses, and optical imaging to capture the evolution of cracking in real time. Experiments were performed using depleted

uranium dioxide (UO_2) pellets, which are useful for collecting valuable data for development and validation of cracking models. A combination of induction and resistance heating was used to create thermal gradients similar to those seen in a reactor environment. Characterization of the pellets was conducted both before and after cracking. The cracking patterns are moderately different than those expected in a typical reactor, due to the variations in the thermal conditions and pellet microstructures. However, when the actual conditions of these experiments are reproduced in computational models with sufficient precision, such out-of-pile testing on UO_2 pellets, provides relevant data for modeling purposes.

Keywords: Uranium dioxide (UO_2), resistive heating, cracking, temperature, dual imaging, grain boundaries

1. Introduction

The behavior of ceramic fuel is significantly affected by fracture,. Early in the life fuel, fracture is primarily caused by thermal stresses. The fission process in the cylindrical fuel pellets causes volumetric heating that, in conjunction with the forced convective cooling on the exterior of the fuel rod, results in an parabolic temperature profile. The significant tensile stresses that this temperature profile causes on the pellet exterior results in crack initiation in fresh fuel. According to Oguma [1] crack closure and reconstitution happens under steady state conditions.

. Typically, nuclear fuel rods are fabricated with initial pellet clad gap to allow space for radial thermal expansion and swelling due to fission products during operation. When the fuel rod power rises, cracking occurs in pellets because of the thermal stresses induces due to the radial temperature gradients, leading to the formation of crack areas in the pellets. These newly formed cracks on the pellet surface are remunerated by reduction in gap area, which increases the apparent

pellet diameter. This is phenomena is known as relocation. Changes in gap size during fuel irradiation primarily affects fuel rod performance including fuel temperature, fission gas release and pellet-clad mechanical interaction (PCMI). [2,3]. For modeling relocation or gap sizes in fuel performance codes it was assumed that there is a certain degree of gap reduction at specific power levels [4,5,6]. Cracking directly impacts fuel relocation which eventually leads to the reduction of fuel temperature. According to Oguma's finite element analyses and experimental studies it was observed that rod power and cracking are directly related. The rod power level was found to range from as low as 30 W/cm to a maximum of 400 W/cm.

For fuel performance codes to be predictive under a wide range of operating conditions, it is important that they faithfully represent all aspects of fuel system behavior via physics-based models. Because of their important role in regard to fuel behavior, improving the models' capability to represent fracture is of high priority in developing such codes. Although significant advances have been made in fracture modeling, limited data available on cracking initiation and propagation are available for direct validation of these models. A U.S. Department of Energy initiative is currently supporting multiple experimental efforts (including the one described herein) to provide improved data for the validation of these models [7], specifically targeting the BISON code [8]. These include out-of-reactor experiments, as well as a series of planned experiments in Idaho National Laboratory's Transient Test Reactor (TREAT).

Developing an experiment that permits capturing of fracture initiation and growth in light-water reactor (LWR) fuel is challenging due to difficulties in both replicating the thermal conditions experienced by the fuel in the reactor and instrumenting the experiment in a way that permits observation of crack growth without compromising those representative conditions. Using resistive heating to replicate the volumetric heating that occurs in the nuclear reactor is attractive

because it permits more extensive instrumentation than would be possible in an in-reactor experiment. This approach is used in the experimental work described herein. One major challenge related to resistive heating is that UO_2 is a semiconductor with very high electrical resistivity at low temperatures. When its temperature is raised, it becomes much more conductive, permitting resistive heating. The experimental apparatus used in this work employs inductive heating to raise the temperature of the UO_2 prior to performing resistive heating.

The primary objective of the research efforts was to build an experimental set up for capturing real time cracking data such as radial temperature distribution and cracking simultaneously in single out-of-pile UO2 pellet under a laboratory simulated transient temperature conditions by using direct resistive heating for volumetric heat generation in the pellet. . The data collected will be used in the validation of UO2 cracking models in BISON. In the meantime, the experimental results were used for successfully validating 2-D UO2 cracking models in BISON [9]. The 3-D cracking models' validation is currently a work in progress.

2. Previous Related Work

In the late 1970s, resistive heating was used in a series of experiments at Argonne National Laboratory [10]. In those experiments, two power supplies operating in parallel were used to pass current axially through a stack of pellets to raise them to a temperature high enough for them to become conductive, then enough current was applied to obtain the desired heating. A low-voltage, high-current power supply (300 V and 300 A) was used in tandem with a high-voltage, low-current power supply (2500 V and 10 A). A high voltage was applied for the initial pre-heating of the pellets. When the temperature increased and the resistance decreased, the current increased until

it reached a limiting value of 10 A, (until the voltage decreased to 300 V), at which time the system provided a constant 300 V with a current of up to 310 A. This system provided rapid heating to replicate reactivity-initiated accident (RIA) conditions. Cooling on the outer surface of the pellets was achieved by flowing cooled helium past the pellet stack. Three pyrometers were used to capture temperatures at different ranges, such as 400–1000°C, 900–1600°C, and 1500–3000°C. The configuration of that experiment did not permit direct observation of crack formation, but acoustic emission techniques were used to detect whenever crack propagation occurred.

Along these lines, in a separate study by Oguma [1], out of pile experiments and analyses were conducted for understanding pellet thermal deformation and in-pile analyses were performed to resolve pellet relocation behavior of fuel rods when under operating conditions. For evaluating cracking behavior of pellet prior to PCI, on-power diameter was measured by implementing an electrically heated PCI simulation of fuel rod assemblies.

The test set-up comprised of simulated fuel rods with a tungsten rod in the center for direct resistance heating, diameter and dimension change measuring devices, data acquisition systems and power controller. The test fuel rod that consisted of a fully annealed Zircaloy-2 cladding (outer dia. = 14 mm), hollow UO2 pellets (density = 93% TD) and a tungsten heater (dia. = 5 mm). The as-fabricated pellet-clad gap sizes were set at 60, 100 and 150 microns as an experimental parameter. It was observed that pellet cracking started at a low rod power of 30 W/cm. This was due to the sharper temperature distribution in the centrally heated pellet, which was more on towards a hyperbolic shape rather than parabolic. The number of cracks were found to vary from two to sixteen at minimum and maximum power levels of 30 W/cm and 400 W/cm respectively.

3. Experimental Setup

The current work utilizes a significantly different configuration than that of the Argonne National Laboratory experiments, allowing for imaging of the top surface of the fuel pellet in order to observe radial crack formation intersecting the pellet surface. The experimental details have been previously reported in [11]. Instead of passing the current axially through the pellets as in the previous work, electrodes were placed on the sides of a single pellet to pass the current transversely across it. This allowed for an unobstructed view of the top surface of the pellet. A unique dual imaging technique was utilized in which an infrared camera captured the pellet's full-field temperature gradient while—simultaneously and in real time—an optical camera system captured physical images of cracks. Also, rather than using a high voltage when performing the initial pre-heating, the present work employs induction heating as a more controlled method for raising the pellets to a temperature at which they become sufficiently electrically conductive.

The experimental apparatus described in [11] was developed specifically for these studies permits in situ imaging of cracks visible on the fuel pellet's top surface and measure the corresponding temperature profiles. This is achieved through the dual imaging system that captures both optical and thermal images of the pellet surface [11]. To simplify the process of calibrating and verifying the instrumentation used in these experiments, it was very helpful to use a non-radioactive surrogate material for the fuel pellets. Ceria (CeO_2) has been widely used in the nuclear industry as a non-radioactive surrogate for UO_2 and because its relevant properties were found to be sufficiently similar to those of UO_2, it was used as a surrogate for the fuel pellets in the initial phases of the present study [12], although the present paper focuses solely on experiments on UO_2.

4. Experimental Conditions for UO_2 Pellet Fracture

4.1. Pellet fabrication

A series of tests was performed, each on an individual pellet with varying conditions. The depleted UO_2 pellets studied herein were fabricated at Texas A&M University with an average theoretical density (TD) of 93.74%, an average diameter of 10.98 mm, and an average height of 9.53 mm. The pellets were sintered at 1790°C for 24 hours in Ar-5% H_2. The furnace used for sintering was a MRF – Materials Research Furnace Serial Number 1211. The furnace is water cooled, tungsten element, tungsten shielded. Ultra-high purity argon with 5% hydrogen was used to reduce the UO2 and ultra-high purity argon to sinter the pellets. There were several bottles used, two bottles of each gas were used and connected in parallel to avoid running out of gas during a sintering. There were four bottles always connected, two UHP argon bottles and two UHP Ar-5% H2. There was no mixing of any gases, either one of the gases was selected at one time. The pellets sintered at these conditions were predicted to be stoichiometric $UO_{2.00}$ when the O/U ratio was computed using the CALculation of PHAse Diagrams (CALPHAD model proposed by Besmann et al. [13].

4.2. Dual heating/imaging

UO_2 pellets were mounted on a custom-built modular test stand machined from Combat® Machinable Ceramics Grade AX05 highest purity hBN available at 99.7%+ boron nitride (BN), which serves as an electrical insulator but is still highly thermally conductive [14]. BN is easily machinable, and the modular design provides the flexibility to connect electrodes and feedthroughs while setting up the test stand. The mechanical tolerances in the test stand also help to address and accommodate the thermal expansion and heat transfer in the pellet while undergoing resistive heating. A custom-made molybdenum tube was used the susceptor material which was custom manufactured by Stanford Advanced Materials (SAM) with ultra-high pure Mo content greater than equal to 99.95%. A schematic of the test stand with all the components present is shown in Figure 1. The dimensions of the important components of the test stand are outlined in Table 1.

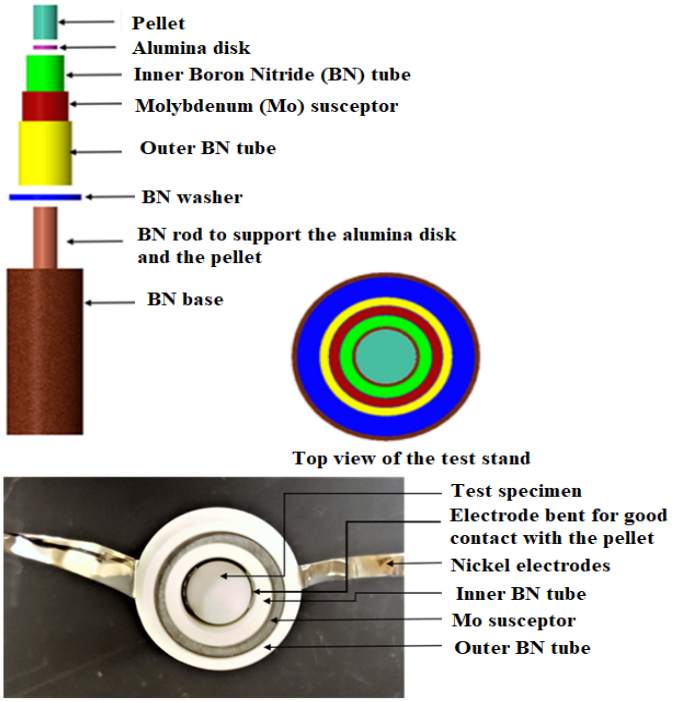

Figure 1. Model of the test stand (top); and the complete assembled test stand showing the electrodes and susceptor (bottom)

Table 1. Dimensions of test stand assembly

Test stand part name	**Dimensions (cm)**
Inner BN tube	I.D. = 1.143, O.D. = 1.5494, H = 2.794
Molybdenum susceptor	I.D. = 1.5748, O.D. = 1.905, H = 2.794
Outer BN tube	I.D. = 1.9304, O.D. = 2.2352, H = 2.794
Ni Electrode	10 X 0.7 X 0.023

In all the tests the vacuum chamber was first evacuated using a rotary vane vacuum pump, and then filled with helium gas that continued to flow through the experimental chamber at a rate of 200 standard cubic centimeters per minute (sccm). The experimental chamber was a custom-built stainless steel ultra-high vacuum 6-way cross with 8" nominal outer diameter, with 10" Outer Diameter, with 5 conflat flanges and one ISO 200 which acted as the door for accessing the test stand inside the chamber.

The oxygen partial pressures (pO2) of the chamber atmosphere were measured by a SETNAG Gen'Air high-precision oxygen analyzer and found to be in the range of 10^{-13} to 10^{-14} atm at 1200°C in a reducing atmosphere. Since the very low oxygen potential in the gas means a very low oxygen content, so it will not change the pellet O/U. Therefore, the pellet retains its stoichiometry during the test as well as predicted by Besmann et al. [13].

During each test, the pellets first underwent induction heating followed by direct resistance heating. The tests began with the DC power supply for resistance heating being set at 0.5 A and 120 V, while the pellet was heated via a molybdenum susceptor using induction heating at 200 A. This was done to raise the pellet to a threshold temperature high enough for it to become sufficiently conductive for resistive heating. The electrical conductivity of UO_2 increases sharply with increasing temperature [15], and the pellets were found to become sufficiently conductive to produce a measurable voltage drop once they reached an average temperature of about 460°C—which, in all the tests, occurred after less than 10 s of induction heating as shown in Table 2. Once a voltage drop was detected, the current was quickly increased to 1 A, and then increased stepwise at 0.5 A increments, along with certain hold times, until a number of different peak currents (e.g., 4 A, 5 A, 6 A, and 8 A) were reached for a given test. This was done to achieve different peak temperatures and to check for any differences in cracking patterns at those resultant currents and

peak temperatures. As expected, the pellets reached different peak temperatures with increasing current; however, the characteristics of the observed cracking did not differ significantly from one test to another.

5. Results and Discussions

5.1. Observed crack initiation

In all the tests, the first evidence of cracking was observed when the current was in between 3.5 and 4 A supplied from the resistance heating power supply. The nominal hold times at each power level, and the hold times until cracking for tests with peak currents of 4 and 8 A, are outlined in Table 2.The maximum deviation in the hold times is 2 seconds for each hold at each power ramp.

Table 2. Peak current values and average hold times

Test no.	Pellet ID	Highest peak current (A)	Nominal hold times at each current level	Induction Heating Times	Hold times and current values for crack initiation	Total time from beginning of test until cracking
1.	U3-38	4.0	42.3 s	8 s	22 s at 3.5 A	111 s
2.	U4-50	4.0	60.0 s	8 s	33 s at 3.5 A	347 s
3.	U5-45B	4.0	43.0 s	4 s	26 s at 3.5 A	244 s
4.	U1-38A	5.0	35.0 s	8 s	30 s at 3.5 A	217 s

5.	U5-26F	6.0	27.0 s	10 s	26 s at 4.0 A	205 s
6.	U5-22C	8.0	25.0 s	7 s	24 s at 4.0 A	182 s
7.	U5-20C	8.0	22.0 s	6 s	2 s at 4.0 A	146 s
8.	U5-20D	8.0	23.6 s	9 s	22 s at 4.0 A	176 s

The test conditions, temperature measurements, cracking patterns, and pellet fabrication details for each of the tests are summarized in Table 3.

Table 3. Test conditions and pellet fabrication details

Pellet ID	**Density**	**Theoretical Density**	**Dimensions**	**Threshold Temperature**	**Maximum Temperature Attained by Pellet**	**Radial Temperature Difference Before Cracking**	**Radial Temperature Difference After Cracking**	**Cracking Patterns**
U3-38	10.52 g/cc	95.86%	D = 11.01 mm, H = 9.14 mm	400°C	1660°C	ΔT_{horiz}^{*} = 310°C ΔT_{vert}^{*} = 485°C	ΔT_{horiz} = 241°C ΔT_{vert} = 196°C	Radial cracks across the

								pellet, radial branching
U4-50	10.31 g/cc	94%	D = 10.96 mm, H = 8.73 mm	450°C	1730°C	ΔT_{horiz}^{*} = 190°C ΔT_{vert}^{*} = 240°C	ΔT_{horiz} = 196°C ΔT_{vert} = 145°C	Radial cracks across the pellet, radial branching
U5-45B	10.36 g/cc	94.45%	D = 10.95 mm, H = 9.33 mm	400°C	1700°C	ΔT_{horiz}^{*} = 230°C ΔT_{vert}^{*} = 280°C	ΔT_{horiz} = 200°C ΔT_{vert} = 160°C	Radial cracks across the pellet, radial branching
U1-38A	10.37 g/cc	94.49%	D = 10.93 mm, H = 9.31 mm	330°C	1800°C	ΔT_{horiz}^{*} = 155°C ΔT_{vert}^{*} = 203°C	ΔT_{horiz} = 176°C ΔT_{vert} = 142°C	Radial cracks across the pellet
U5-26F	10.37 g/cc	94.5%	D = 10.98 mm, H = 9.29 mm	450°C	1860°C	ΔT_{horiz}^{*} = 235°C ΔT_{vert}^{*} = 280°C	ΔT_{horiz} = 354°C ΔT_{vert} = 281°C	Radial cracks across the pellet, radial branching
U5-22C	10.31 g/cc	93.96%		550°C	2100°C	ΔT_{horiz}^{*} = 165°C		Radial cracks

			D = 10.97 mm, H = 9.32 mm			ΔT_{vert}^{*} = 215°C	ΔT_{horiz} = 180°C ΔT_{vert} = 109°C	across the pellet, radial branching
U5-20C	10.27 g/cc	93.61%	D = 1.098 mm, H = 9.34 mm	500°C	2100°C	ΔT_{horiz}^{*} = 122°C ΔT_{vert}^{*} = 190°C	ΔT_{horiz} = 208°C ΔT_{vert} = 140°C	Radial cracks across the pellet, radial branching
U5-20D	10.23 g/cc	93.28%	D = 11.01 mm, H = 9.32 mm	600°C	2100°C	ΔT_{horiz}^{*} = 206°C ΔT_{vert}^{*} = 266°C	ΔT_{horiz} = 214°C ΔT_{vert} = 135°C	Radial cracks across the pellet

ΔT_{horiz}^{*} is the temperature difference along the line profile drawn between the electrodes.

ΔT_{vert}^{*} is the temperature difference along the line profile drawn perpendicular to the horizontal line across the non-electrode side.

Experiments were conducted at different peak current levels to study any differences in cracking patterns and radial temperature profiles. Three tests were performed at both the 4 and 8 A peak current values, whereas one test each was conducted at intermediate peak currents of 5 and 6 A. Tests were conducted at higher peak current values greater than 4 A to check for any change in

cracking patterns at higher current values. However, no significant change was observed in the cracking patterns at those higher power levels beyond what observed when cracking first initiated at the 3.5-4 A power level. The only major difference in behavior under higher power is that higher peak temperatures were attained, which are reported in Table 3. Figure 2 shows a current-voltage-time plot for one of the tests. Voltage decreases sharply when the pellet becomes sufficiently conductive from the inductively heated susceptor, and the ramp in current from the resistive heater induces volumetric heating in the pellet, creating a radial temperature gradient within the pellet.

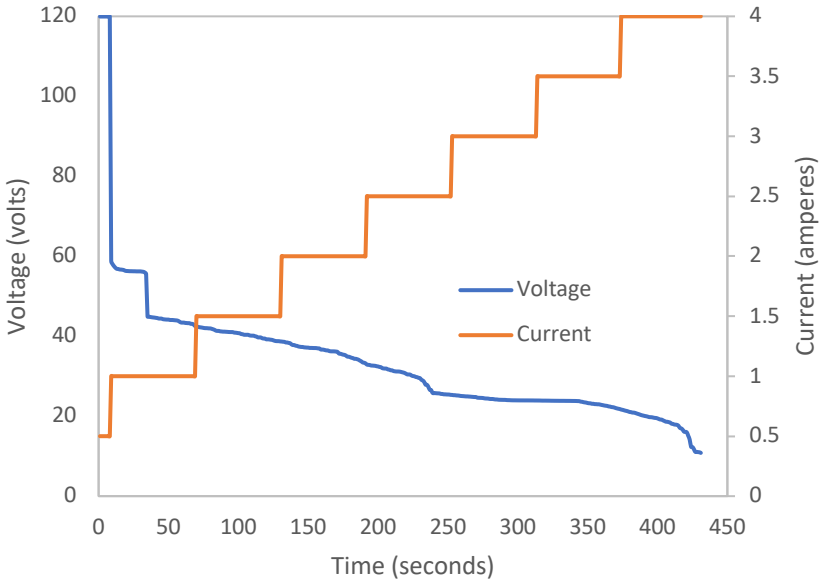

Figure 2. Current (secondary y-axis on the right) and voltage (primary y-axis on the left) for the resistive heating of pellet U4-50 as a function of time; the pellet becomes conductive after about 4 s of induction heating

5.2. Infrared and optical imaging

The infrared camera from FLIR Systems, Inc. has a very high thermal sensitivity of <20 mK, so even slight changes in surface temperature during the test are captured. Full-field temperature

distributions for UO_2 pellets bearing pellet IDs U4-50, U5-26F, and U5-22C both before and after cracking are shown in this section in Figures 5 and 6 respectively. Infrared images for U4-50 both before and after cracking were captured after 305 and 339 s of resistive heating, respectively. Similarly, for U5-26F, infrared images both before and after cracking were captured at 168 and 195 s, respectively. Along those same lines, for U5-22C, infrared images both before and after cracking were captured after 150 and 175 s, respectively. The infrared images, temperature plots, and optical images of the pellets both before and after cracking are shown respectively in Figures 5 and 6 for selected cases involving low, intermediate, and high peak currents (4 A, 6 A, and 8 A). To facilitate comparisons among the various experiments and between simulation results, temperature profiles for each of these experiments were extracted along two lines: one passing horizontally through the electrodes (shown in green on the infrared images in Figures 3 and 4), and one perpendicular to that line in the vertical direction in this image (shown in blue in those same figures). These temperature profiles are shown in Figures 5 and 6 for the same three experiments shown in Figures 3 and 4.

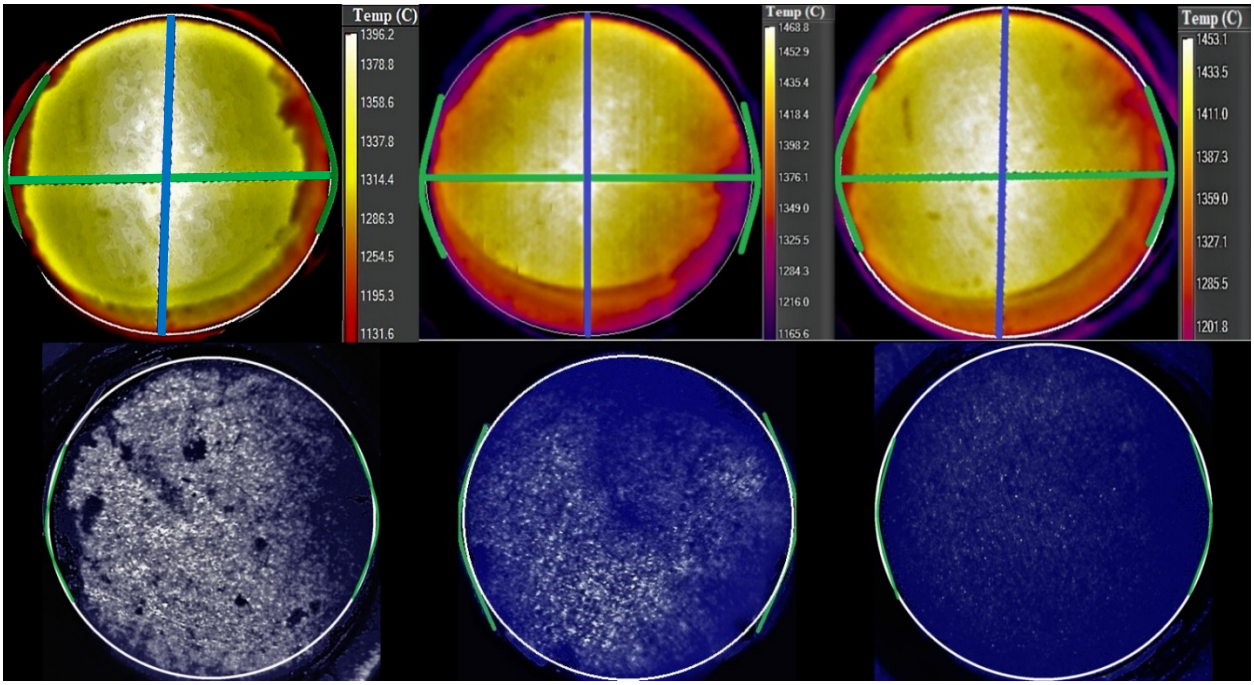

Figure 3. Infrared (top) and optical (bottom) images of UO_2 pellets prior to cracking at low, intermediate, and high peak currents of 4 A (left), 6 A (middle), and 8 A (right), respectively. Pellet boundaries are marked by white circles, and electrodes are marked by green arcs. (From left to right: UO2 pellet IDs: U4-50 [4 A], U5-26F [6 A], and U5-22C [8 A])

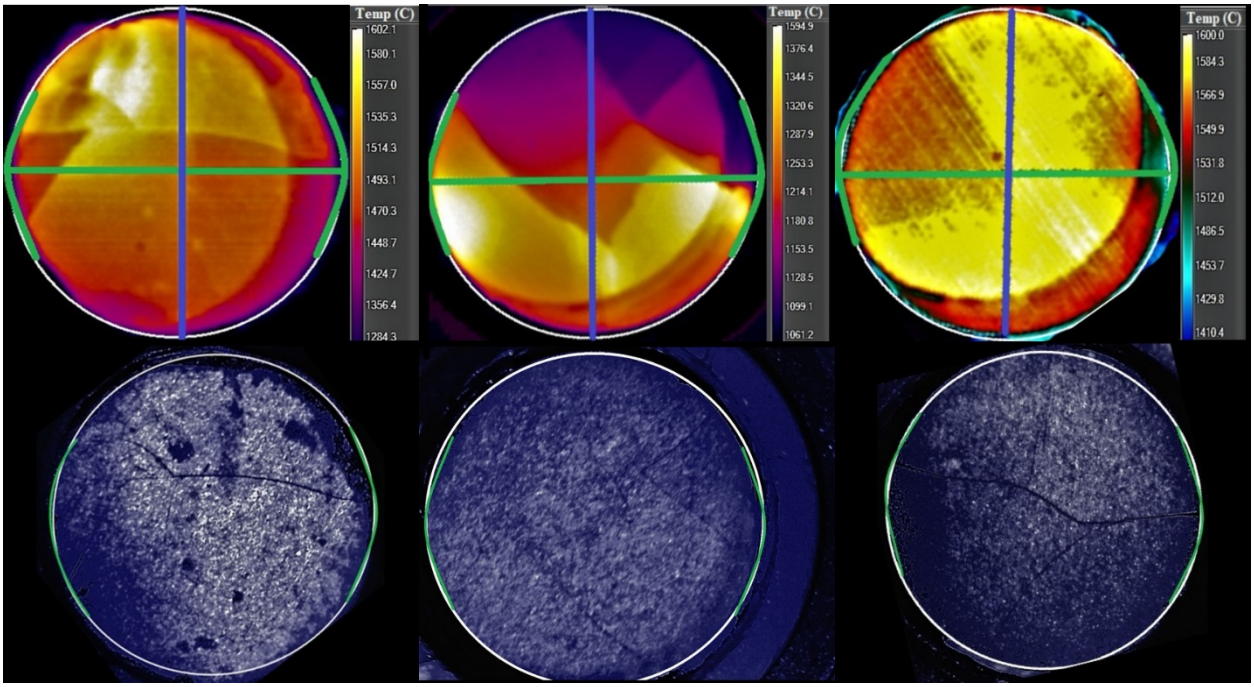

Figure 4. Infrared (top) and optical (bottom) images of UO_2 pellets after cracking at low, intermediate, and high peak currents of 4 A (left), 6 A (middle), and 8 A (right), respectively. Pellet boundaries are marked by white circles, and electrodes are marked by green arcs. (From left to right: UO2 pellet IDs: U4-50 [4 A], U5-26F [6 A], and U5-22C [8 A].)

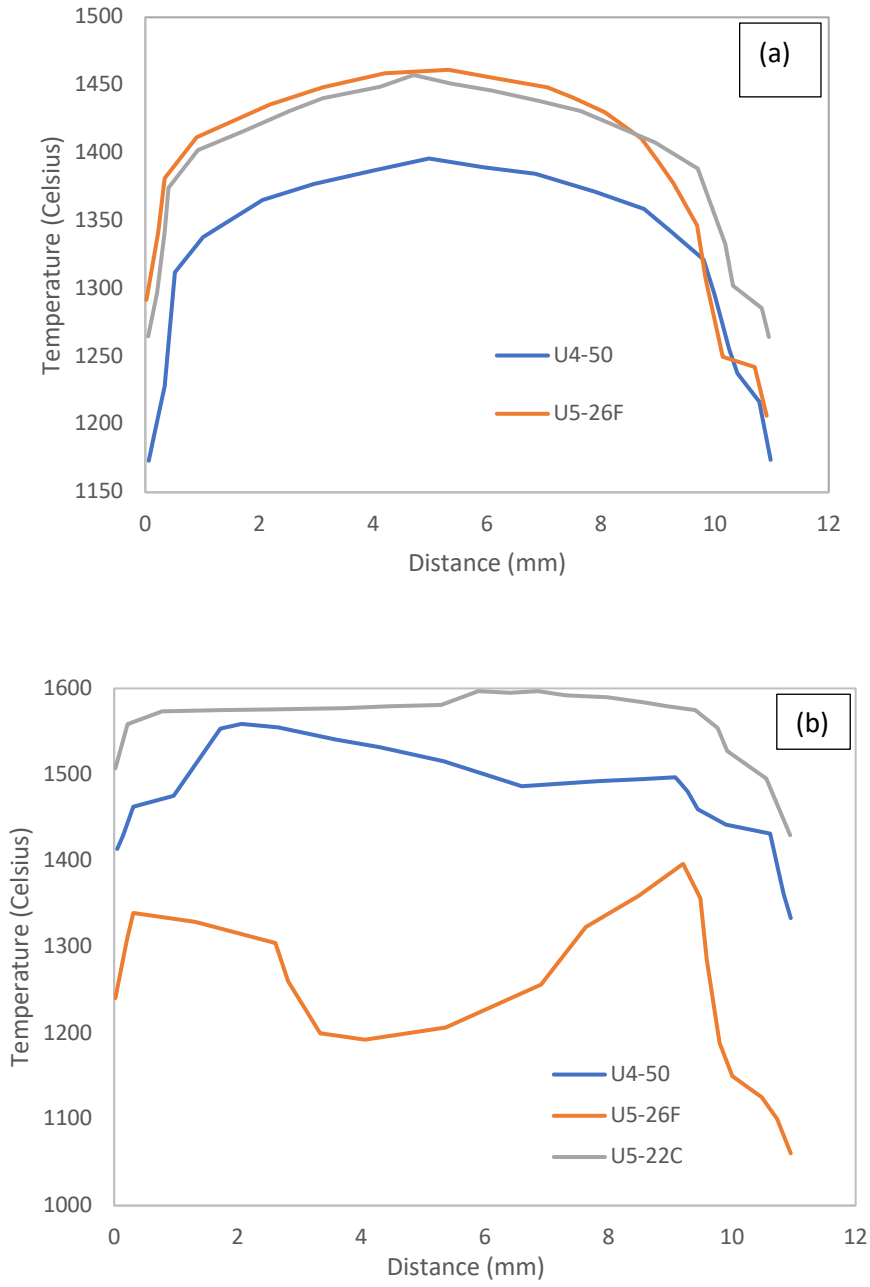

Figure 5. Horizontal temperature profiles along the top surfaces of three UO_2 pellets before (a) and after (b) cracking at low, intermediate, and high peak currents of 4 A, 6 A, and 8 A, respectively: U4-50 (4 A), U5-26F (6 A), and U5-22C (8 A).

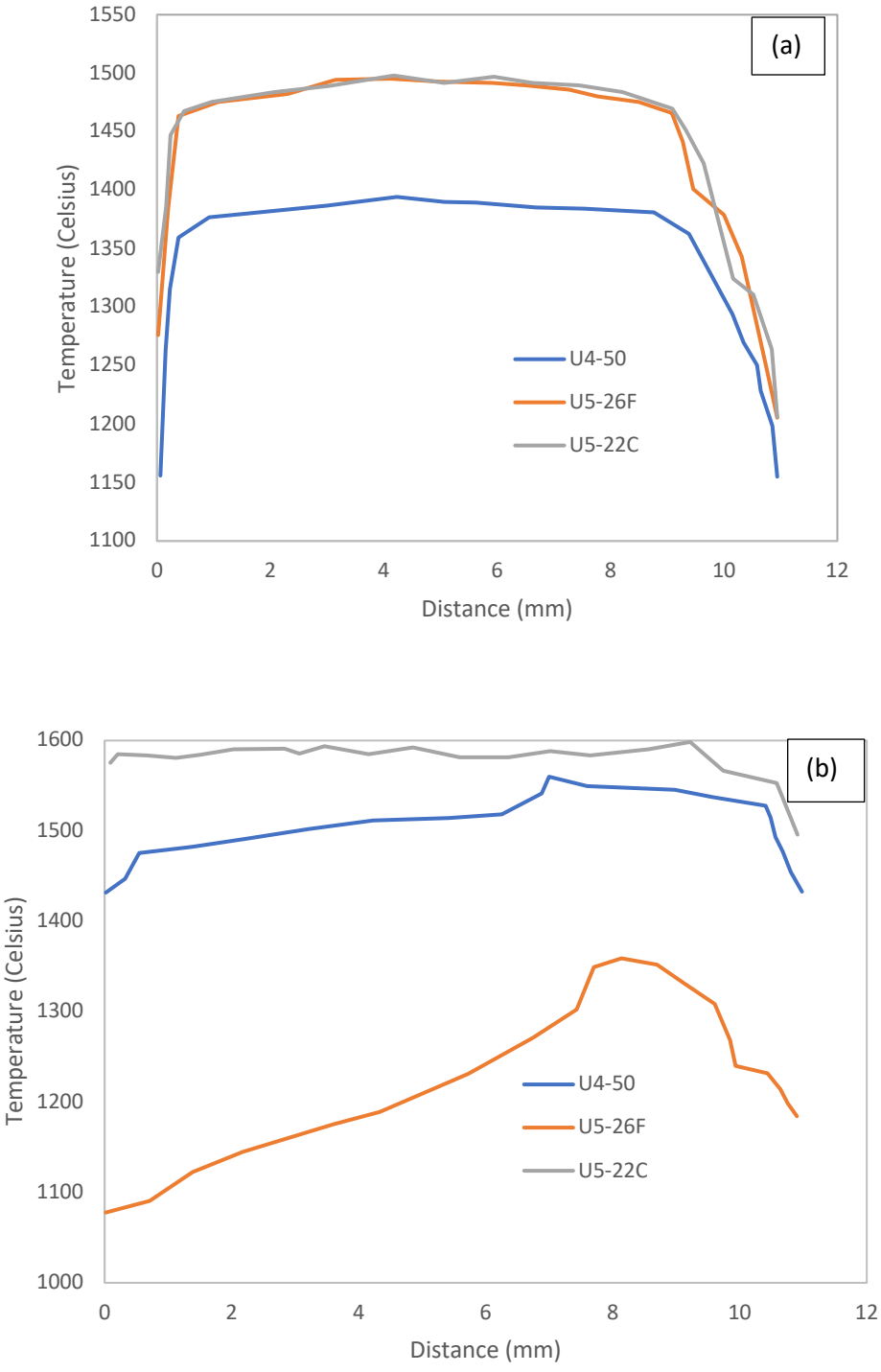

Figure 6. Vertical temperature profiles along the top surfaces of three UO_2 pellets before (a) and after (b) cracking at low, intermediate, and high peak currents of 4 A, 6 A, and 8 A, respectively: U4-50 (4 A), U5-26F (6 A), and U5-22C (8 A).

From both the full-field and line plots, the temperatures are seen to be smooth and continuous prior to cracking. However, once cracking occurs, significant discontinuities arise at the crack locations, due to the significant thermal and electrical resistance at the gaps. The average radial temperature differences prior to cracking were measured to be 201.6 and 270°C along the horizontal and vertical lines, respectively. Prior to cracking, there is a larger difference between the centerline and outer-surface temperatures along the vertical line than what is observed along the horizontal line. However, this pattern reverses after cracking primarily since the direction of current changes after crack formation. Cracking causes change in the electrical resistance in the pellet and the direction of flow of current as well. Since the current follows the path of least resistance, the temperature distribution across the pellet also changes i.e., the temperature difference along the horizontal line becomes greater than what is observed along the vertical line. The infrared data show that cracks initiate at when the difference between the peak (centerline) and surface temperature is on average 221 and 163.5°C along the horizontal and vertical lines, respectively.

It is to be noted that, the pellet peak temperatures were measured around the center of the pellet which was also the centerline temperatures before cracking happened as seen in Figures 5(a) and 6(a) respectively along the horizontal and vertical directions of radial temperature measurements in the pellet. However, at the onset of cracking, this changes. Cracking is an extremely fast process, and as soon as cracks initiate and propagate the temperature distribution changes significantly across the pellet. The pellet peak temperatures are no longer concentrated particularly at the center of the pellet rather they are distributed at various “hot-spots” portions in the pellet. The main reason for this observation was due to the fact that, after cracking the electrical contact of the pellets with the electrodes changes leading to imperfect contact which is opposite to the way it was prior to cracking. This improper contact results in non-uniform current flow in the

pellet. As a result, the parts of the pellet which are in good contact has good current flow leading to higher temperature distribution in those areas only relative to the other parts of the pellet which are in improper electrical contact with the electrodes and thus relatively lower temperatures as well.

More importantly it was observed that cracks first initiate when the pellet peak temperature is about 1600°C and that the radial temperature differences obtained in these experiments (200°C average) is much less to what is observed in a typical reactor (700-800°C). The primary reason is because of the way the pellet is cooled. The pellet is cooled by means of turning off the resistive heating power supply, resulting in significant radiative heat losses from the top radial surface of the pellet into the chamber and purging helium (0.20 l/min) inside the vacuum chamber instead of passing it right over the pellet. The primary objective of the study was to obtain radial cracking images and radial temperature distribution on the pellet surface simultaneously in-situ for validation of UO2 cracking models. Therefore, there was a need of having an unobstructed view of the pellet surface. So, it was not possible to flow helium gas directly on top of the pellet to cool the surface using any form of feedthrough or instrumentation that will not block the view of the pellet radial surface from the top. Moreover, the helium purged inside the chamber was also at a very low flow rate so as not to damage the oxygen analyzer which had a maximum flow rate capacity of 0.20 l/min for measuring oxygen partial pressures at the optimum accuracy levels.

Additional factor responsible for the low ΔT and higher cracking temperatures was the low convective and radiative heat transfer coefficients. The layers of the annular cylinders and gaps in the test stand surrounding the pellet, along with the natural convection, act as a set of resistors in series. By calculating the Nusselt number, Prandtl number and Grashof number, the total heat

transfer coefficient was found to be significantly low which was responsible for causing the pellets to crack at relatively low ΔT and higher peak temperatures than typical LWRs [16].

Another interesting observation from the infrared images was how cracking affects the temperature profiles observed on the top of the pellet after cracking. Prior to cracking, the spatial temperature distribution is continuous, with a hotter centerline temperature and cooler surface temperature prior to cracking. However, as cracks initiate and propagate—an extremely fast process—the temperature profile changes rapidly and develops strong discontinuities. The thermal images show the pellets being divided into zones that have relatively uniform temperatures within each zone, with large temperature jumps on the boundaries of these zones. Typically, one of these zones becomes hotter than the others, separated by the major primary crack along the pellet diameter. This behavior is largely due to the high resistance to heat transfer caused by the cracks. The large temperature differences between these zones causes large differences in the thermal and electrical conductivity, which is, in turn impacted by cracking and temperature [17, 15]. Cracking also affects the electrical fields because it causes poor contact between cracked zones and between the electrodes and the pellet. It should be noted that, in multiple ways, the cracking pattern and temperature profiles obtained in these experiments differ from what would be observed in a typical reactor environment. Some key differences are as follows:

1. The pellets tested in this study on cracking have a low average TD of 93%, which is lower than the 95–96% TD typically observed in standard commercial reactor fuels. Density varies directly with electrical conductivity. Thus, a low-density pellet, has lower electrical conductivity, which means under resistive heating it takes longer to attain the peak temperatures needed for cracking [18].

2. Typically, in a LWR, the pellet surface is about 400–500°C and the centerline temperature about 1200°C (ΔT = 700–800°C) while operating under steady-state conditions [19]. Immediately after the fuel rod power increases and before any significant swelling or creep can occur, a network of cracks due to thermal stresses is induced by the radial high-temperature gradients (a few hundred Celsius per centimeter) [20]. However, in the present study, by means of resistive heating and volumetric heat losses, an average maximum radial temperature difference of 200°C was generated in the pellet. This ΔT was used to quantify the corresponding linear heat rate (LHR) by using the equation, $q' = 4.\pi.k.\ \Delta T$, where q' is the linear heat rate in W/cm, k is the thermal conductivity in W/m-K and ΔT is the temperature difference. Based on this calculation, for the present study it was found out that the LHR for ΔT= 200°C was found to be 178 W/cm and number of radial cracks observed was between 2 and 4 for all the pellets. This matches well with the predictions made by Oguma [1] where the maximum number of cracks was four for LHR ranging from 0 to 200 W/cm.

   This temperature difference of 200°C was enough to create thermal stresses in the pellet, causing it to crack. This aligns with the fracture model suggested by Su Faya in [21], as well as the preliminary BISON simulations [8]. Both [21] and [8] concluded that a temperature difference of 150°C was sufficient to induce thermal stresses and initiate cracking in the fuel pellet.
3. As previously mentioned, because of the way that the current is passed transversely across the pellets, the temperature contours in these experiments are oblong, which results in stress concentrations and fracture initiation near the electrodes, which differs from the expected

behavior in the LWR environment, where radial cracks would be spread more uniformly around the pellet periphery.

4. The high temperature gradients of the pellets in fresh LWR fuel are caused by volumetric heating and radial heat rejection. However, over the life of the fuel, the microstructure changes in a nonuniform way due to radial variations in temperature, grain size, porosity, local burn-up, and fission product chemistry [22,23]. This study is relevant to fresh LWR fuel but does not address burnup-dependent phenomena that would affect late-life fracture behavior.

Despite the differences between the environment and conditions created by the resistive heating tests and the nuclear reactor, the results of the current research effort still provide data that is useful for validation of computational models. As long as the computational models can replicate the experimental environment, these experiments can be used for validation of those models. The experimental data has been used in a parametric study conducted by Yeh et al. [9] encompassing electrical conductivity and heat transfer coefficients where the temperature and cracking data from these experiments were successfully implemented in validating the 2-D cracking model in BISON.

In all eight experiments, it was observed that the temperature gradient across the non-electrode side (vertical blue line) was higher than across the electrodes (horizontal green line) prior to crack formation as seen in Figures 5 and 6. This temperature gradient resulted in every case in the formation of a major radial crack that extended across the pellet diameter, with smaller radial cracks branching out of it. Video generated by stitching optical images captured during the tests at every 1 second interval shows that the cracks originated at either one of the electrodes before propagating radially across the pellet as seen in Figure 7.

The optical images immediately prior to cracking, at the point of crack initiation, and after propagation, are shown in Figure 7 for pellet U4-50.

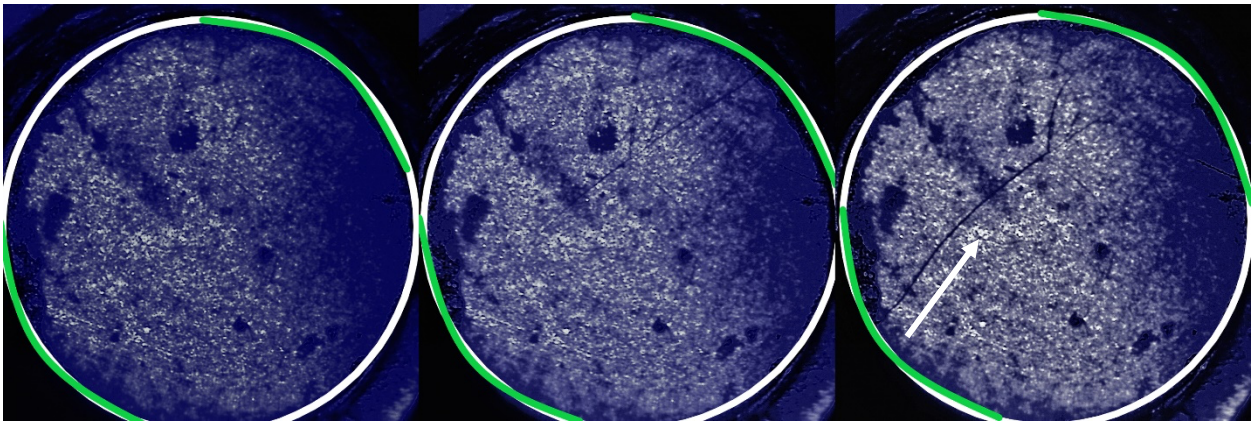

Figure 7. U4-50 pellet, showing cracking. The images show the moment before cracking (left), the first crack initiation at the electrodes (center), and crack propagation (right). The pellet boundary is marked by a white circle, and the electrodes are marked by green arcs. In this case, the point of cracks initiation has been marked by white arrow

The time stamps on the optical images were used to determine the current and voltage at the exact moments when cracks initiated. After comparing the optical images of cracking with the thermal data, the first cracking event was confirmed to have occurred at about 1600°C centerline temperature, when the current was between 3.5 and 4 A.

Figure 8 clearly shows that in addition to the radial cracking observed on the top surfaces during the experiment, there is also significant axial cracking, typically manifested as a single major crack at the pellet mid-plane.

Figure 8 (a)–(h) shows side views of the pellets after being removed from the test chamber.

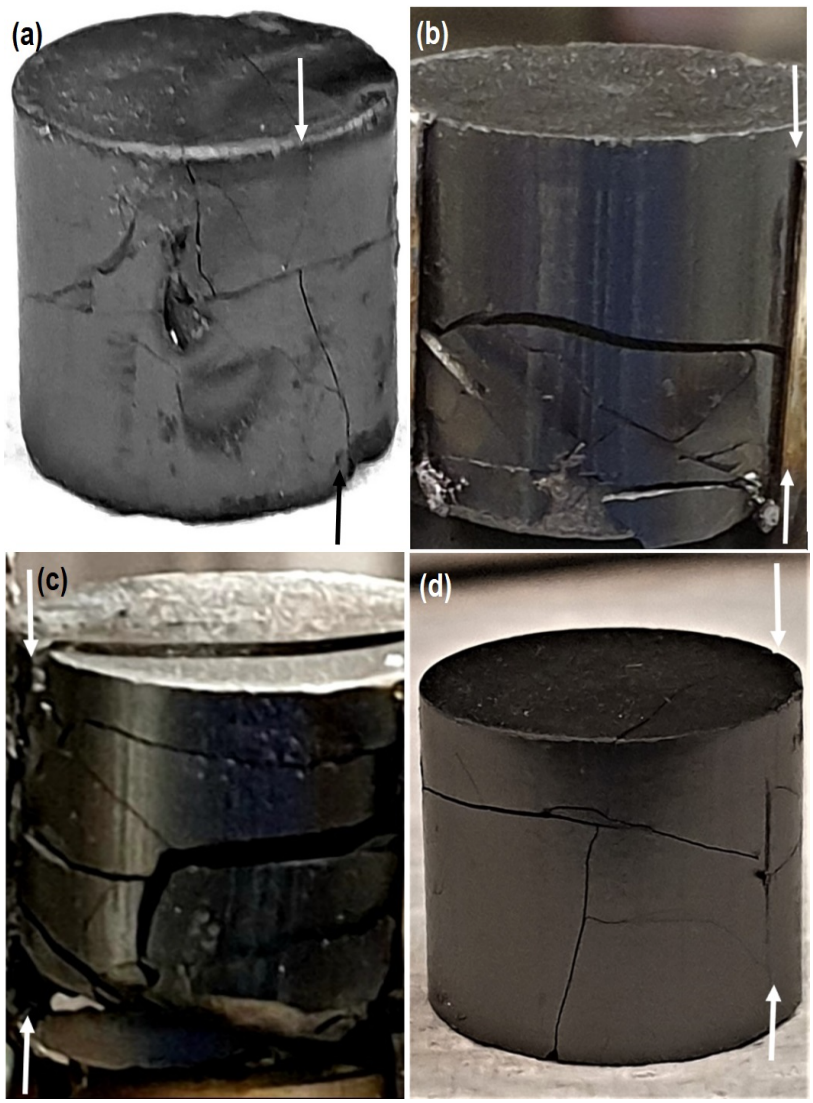
(a)
(b)
(c)
(d)

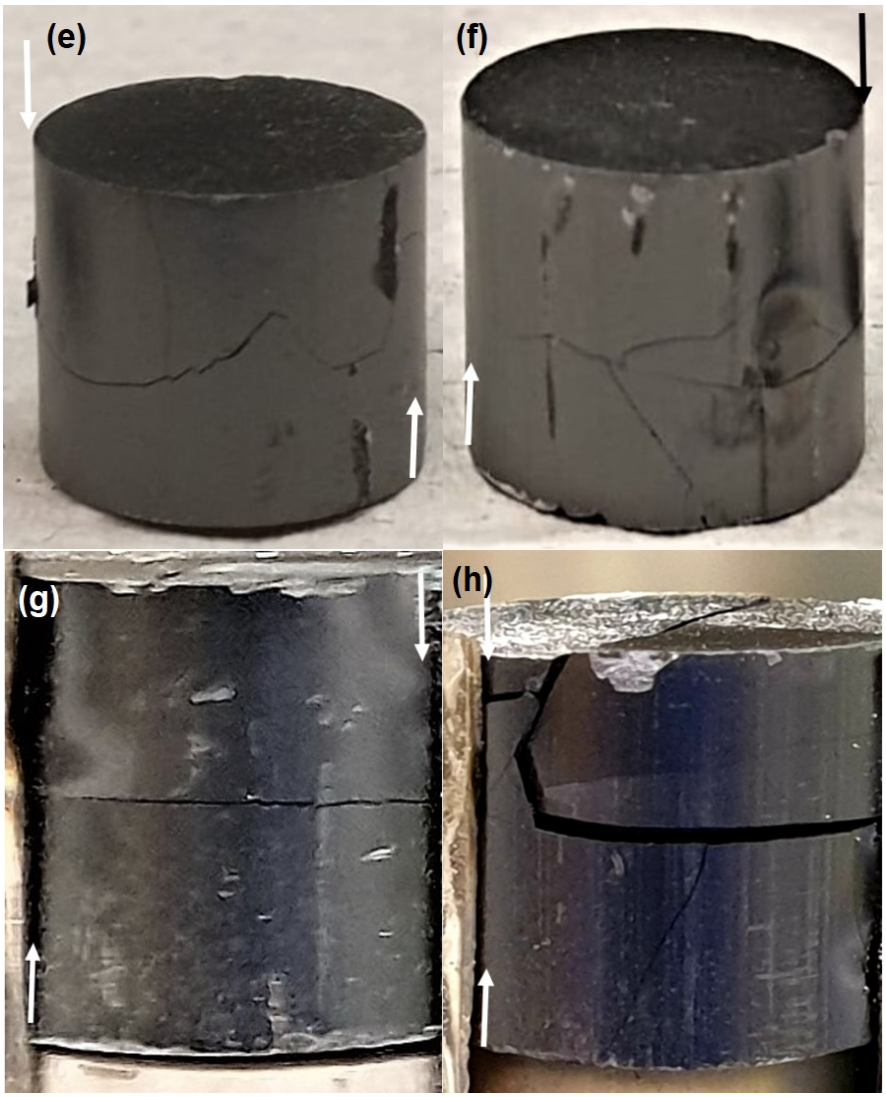

Figure 8. Side views of UO_2 pellets after removal from test stand, showing axial cracking: (a) U4-50, (b) U5-45B, (c) U3-38, (d) U5-26F, (e) U5-22C, (f) U5-20C, (g) U1-38A, and (h) U5-20D. The black and white arrows in the above image represent the positions of electrodes around the pellets.

Since the current is passed transversely across the pellet, there is significant spatial variation in the current density across the pellet cross-section. Preliminary two-dimensional (2D) BISON simulations conducted by Yeh et al. [9] show that the temperature contours of the experiments conducted in this study were oblong as opposed to the circular shape that would be seen in a reactor

environment. Because of the nature of these oblong temperature contours and the resulting thermally induced stresses, Yeh et al. [9] predicted that most radial cracks would initiate near the electrodes and propagate inward, while axial cracks would initiate at azimuthal locations at 90° angle with respect to the electrodes.

These 2D simulations are cross-section models that do not capture axial temperature variations. Because there is a path for convective as well as radiative heat loss from the top surface of the pellet into the test chamber, the axial thermal gradients could be significant. The maximum heat loss in the pellet is from the top which creates an axial temperature gradient. As a result, the top of the pellet is cooler than the bottom. The actual amount of heat loss can be quantified using three-dimensional (3D) representations of the pellet, which is currently a work in progress. This thermal gradient as shown in Figure 9, drives the radial cracks to propagate axially until they meet the axial cracks, at which point the pellet is completely fractured.

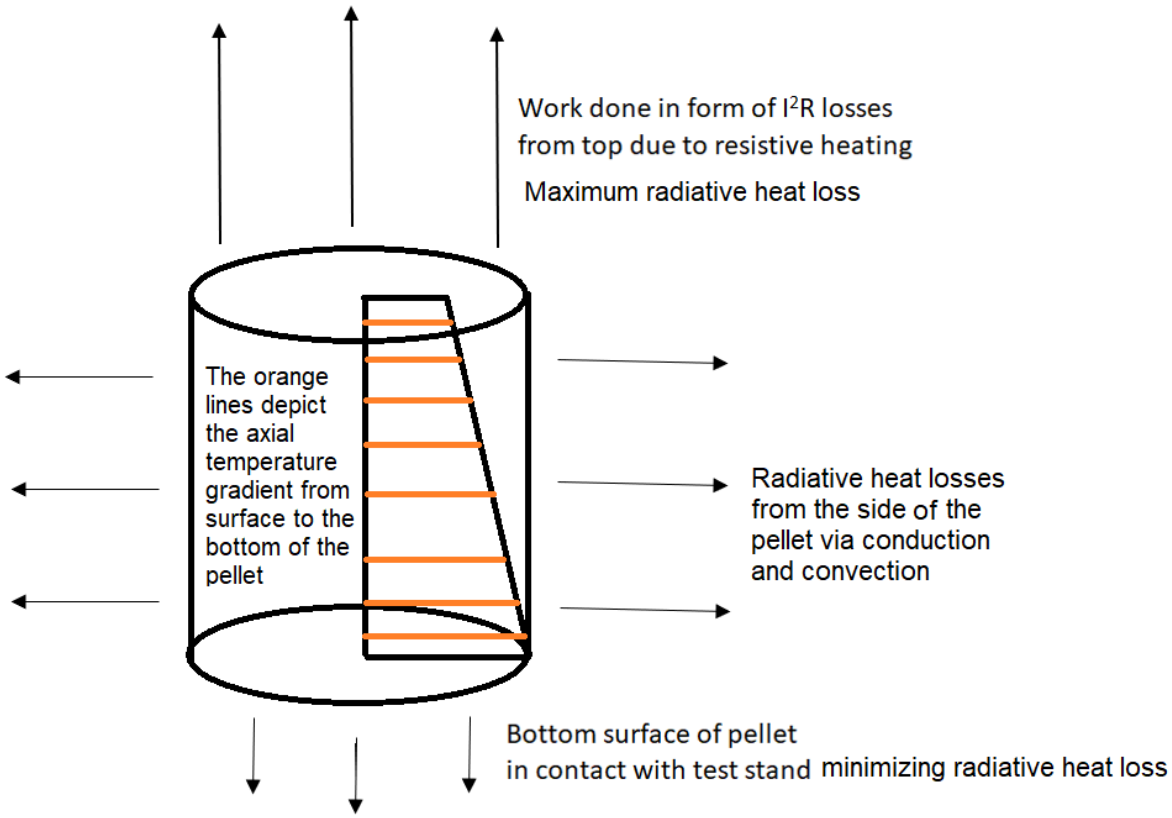

Figure 9. Schematic showing how heat loss from the top surface results in an axial temperature gradient in the pellet. The size of the arrows around the pellet show the relative magnitude of heat losses from the various surfaces. The larger arrows show the maximum radiative heat loss is from the top surface of the pellet, followed by intermediate losses from the sides and the minimum heat loss is at the bottom surface of the pellet.

The formation of significant axial cracks in the experiments as shown in Figure 8, is reasonably consistent with the predictions of Yeh et al. [9]. As previously mentioned, those simulations employed 2D planar models, and only predict the extent of axial cracking at a given location in the cross-section, and not the number or location of axial cracks along the axis of the pellet. However, the 2D planar models did predict axial cracking that penetrated deeply into the pellets.

Future 3D modeling efforts would be necessary to determine whether fracture models predict the number and axial locations of axial cracks.

The time history of the peak temperatures for the three pellets namely U4-50, U5-26F and U5-22C are shown in Figure 10. There is a rapid rise in temperature in the inductive heating phase until the pellet gets sufficiently conductive to allow resistive heating. Thereafter, the temperature increases stepwise with ramp in current at each power level. The various hold times can also be inferred from Figure 10 as well, which have also been reported in Table 2.

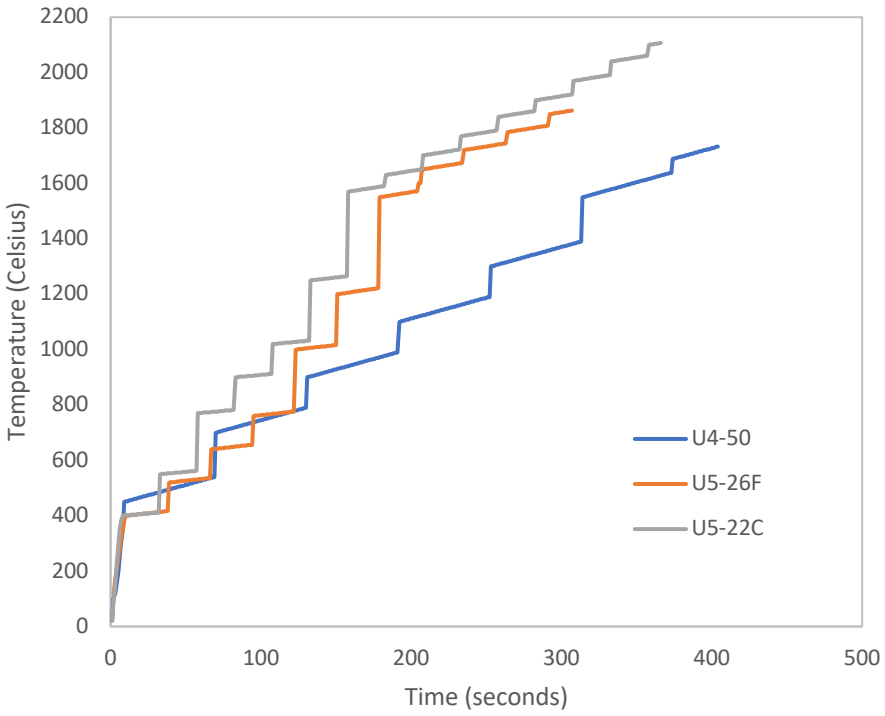

Figure 10. Time history of peak temperatures for pellets U4-50, U5-26F and U5-22C

To use the results from these experiments for validation of computational models, it is important to ensure that a model accurately represents the thermal conditions prior to cracking. This is challenging because it requires accurately representing both the electrical and thermal fields, which

are affected by boundary conditions and temperature-dependent material properties. To facilitate calibration of numerical models, the temperature profiles along the horizontal and vertical axis for one of the experiments (pellet U5-22C) at a number of points in time during the resistive heating process are shown in Figure 11. This pellet became sufficiently conductive for resistive heating at 8 s when the temperature reached 550°C, and thereafter it was heated until 181 s without any evidence of cracking. Cracking was first observed at 182 s, when the peak temperature was about 1600°C. The total heating time of the pellet was 366 s, which included inductive and resistive heating, during which it attained a peak temperature of 2100°C.

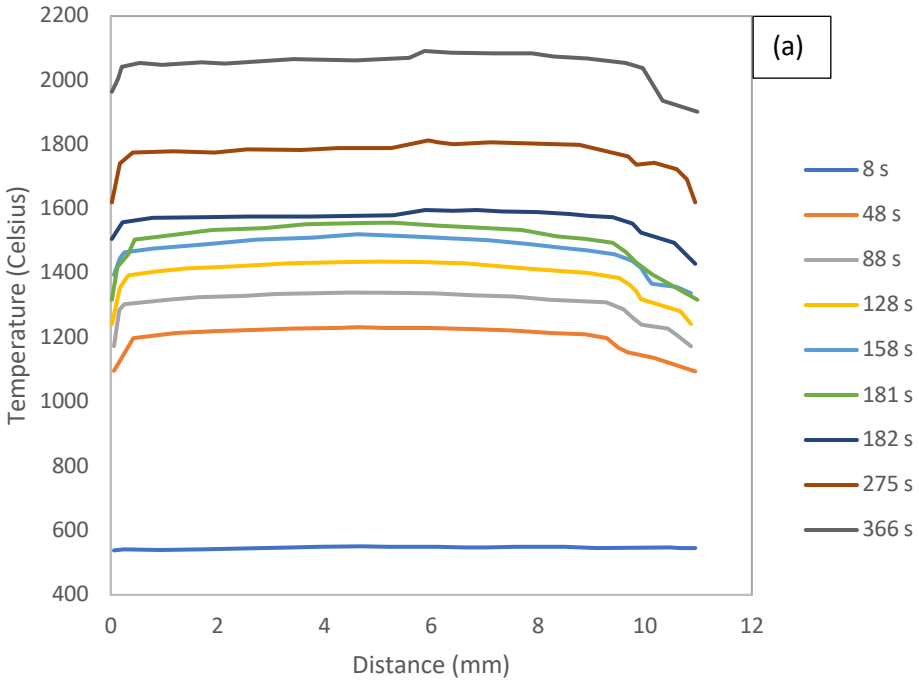

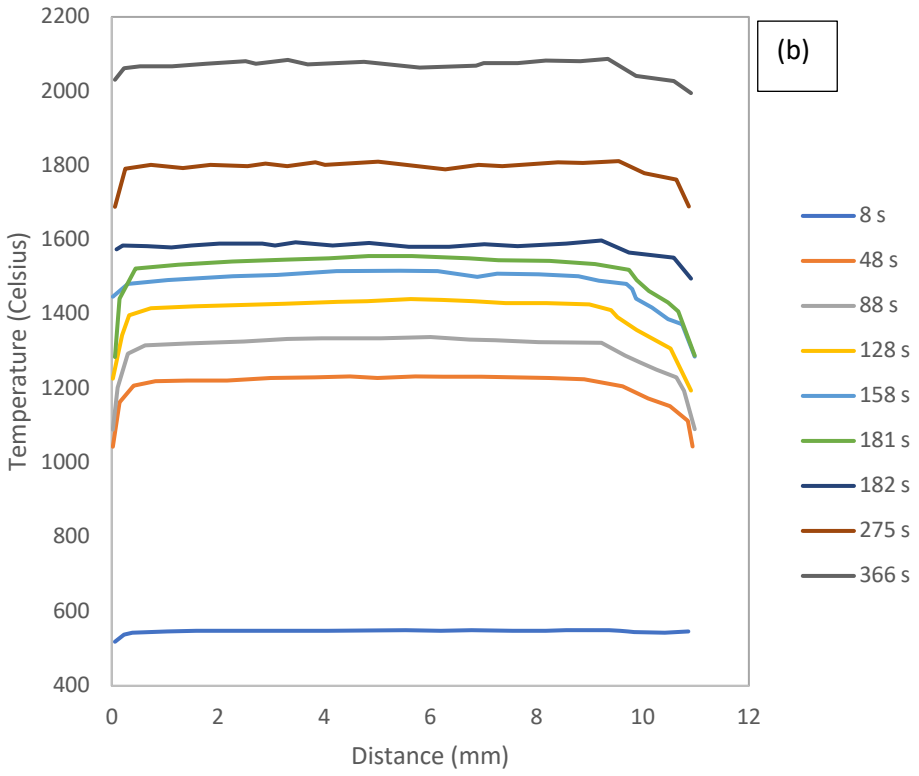

Figure 11. Temperature profiles for pellet ID U5-22C along the (a) horizontal and (b) vertical axis at various points in time during the resistive heating phase of the experiment

6. Characterization of UO_2 Pellets

The cracked pellets from the experiments were further characterized as described here to better understand the microstructural changes and mechanisms driving the formation and propagation of cracks. This characterization included microscopy and measurements of electrical conductivity.

6.1. Microscopy

Optical and scanning electron microscopy (SEM) were performed on as fabricated and cracked UO_2 pellets. Optical microscopy of chemically etched pellets showed distinct grain boundaries and

grain sizes in the bulk of the pellets. Each sample was sectioned and then mounted in epoxy, followed by grinding and polishing. Next, it was chemically etched using a solution comprising of 10 ml 95% sulfuric acid (H_2SO_4) and 90 ml of 30% hydrogen peroxide (H_2O_2) [24]. The sample was initially etched for 10 s, then the etching was continued at 20 s increments until the grain boundaries became clearly visible. The optical microscopy and SEM images of an etched pellet are shown in Figures 12 and 13, respectively.

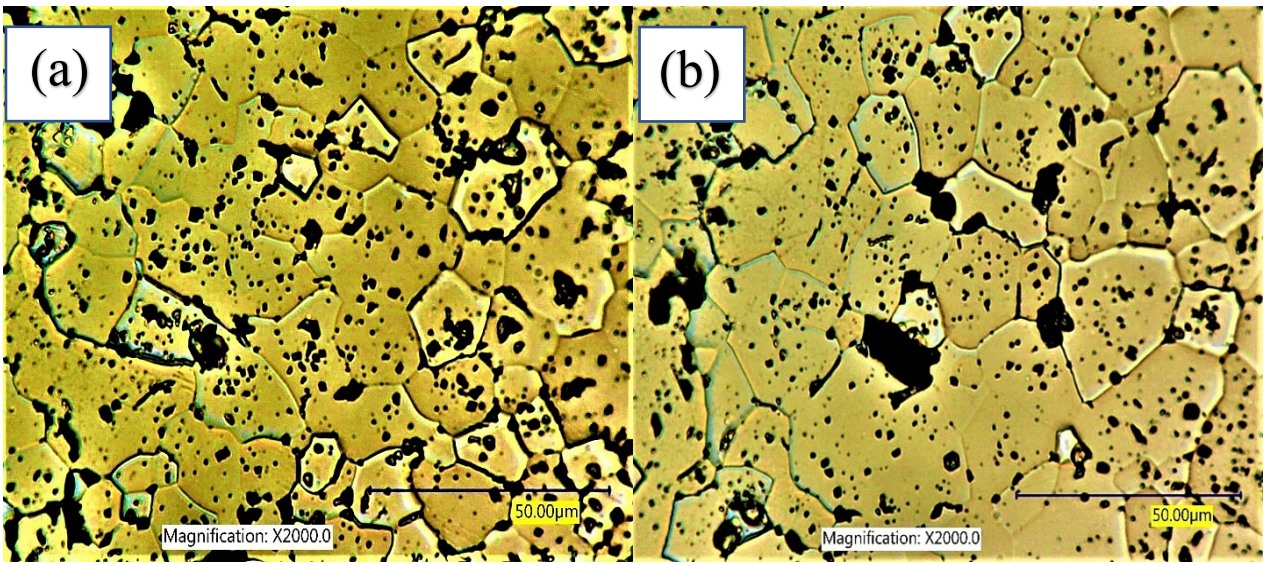

Figure 12. Optical microscopy image of a chemically etched pellet, showing grain boundaries at the center (a) and edge (b) under polarized light

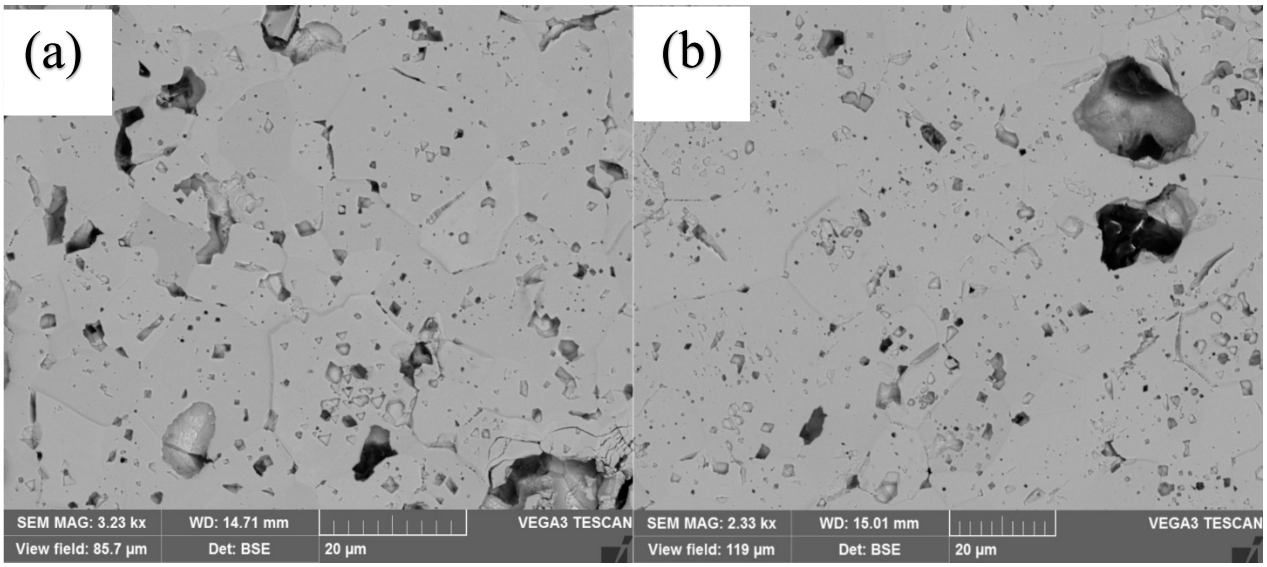

Figure 13. SEM image of etched UO_2 pellet, showing grain boundaries at the center (a) and edge (b)

Since this pellet was thermally etched during the sintering process, SEM imaging of the as-fabricated pellet surface revealed well-defined grain boundaries, as shown in Figure 14. The pellet was sintered at 1790°C for 24 hours in Ar-5%H2. The sintering atmosphere is usually reducing, with some percentage of hydrogen (H_2) gas for obtaining $UO_{2.00}$. The H_2 helps to reduce the uranium in order to maintain stoichiometry. The reducing H_2 atmosphere removes the excess O_2 and maintains a controlled oxygen atmosphere resulting in a chemical oxygen potential of −75 to −125 kJ/mole which causes thermal etching in the pellet [25]. Generally, thermal etching is very superficial and cannot penetrate to the bulk of the pellet. As a result, we observe the well-defined grains on the as-fabricated surface only, not in the bulk after the pellet has been cut or sectioned [22].

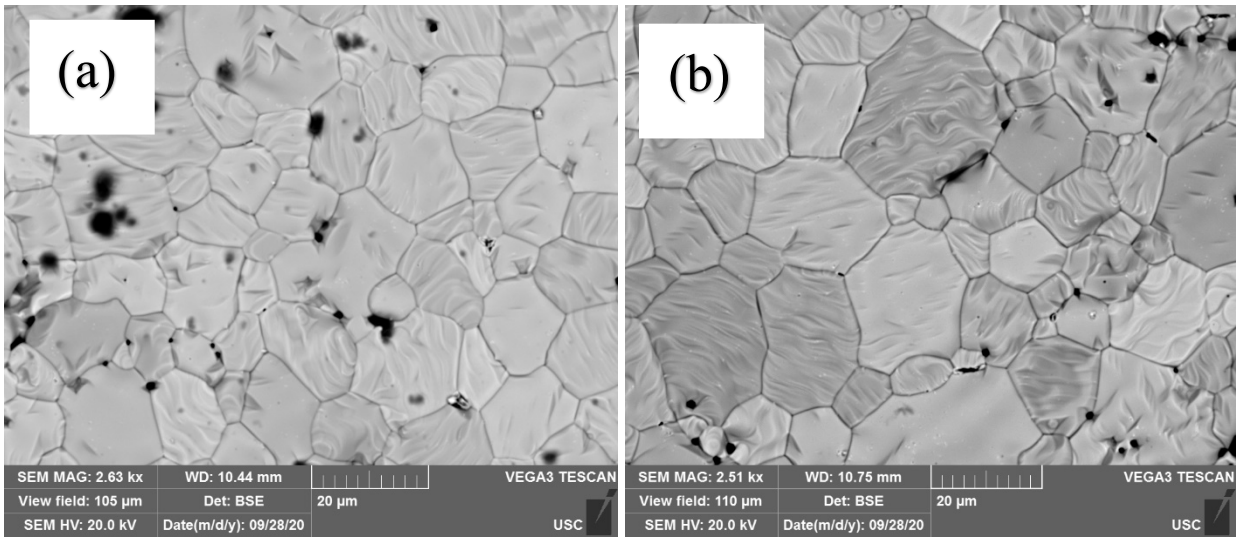

Figure 14. SEM image of an as-fabricated pellet surface, showing well-defined grain boundaries at the center (a) and edge (b) due to thermal etching; the black spots within the grains are impurities or inclusions and the ones on grain boundaries are pores

Chemically etched surface in Figure 14 shows similar grain structure and grain sizes as the as fabricated surface shown in Figure 16. These micrographs reveal that the UO2 pellets have a grain size of approximately 14 microns which is very typical of standard LWR pellets.

Furthermore, the cracked surfaces were examined using SEM, revealing details about the sequence of crack formation and propagation. Images of the cracked surfaces of pellets U4-50 (4 A), U5-26F (6 A), and U5-20C (8 A) after undergoing resistive heating, cooling, and removal from the test stand are shown in Figures 15, 16, and 17, respectively. The regions of interest investigated have been marked by black boxes and the corresponding macroscopic view has been shown.

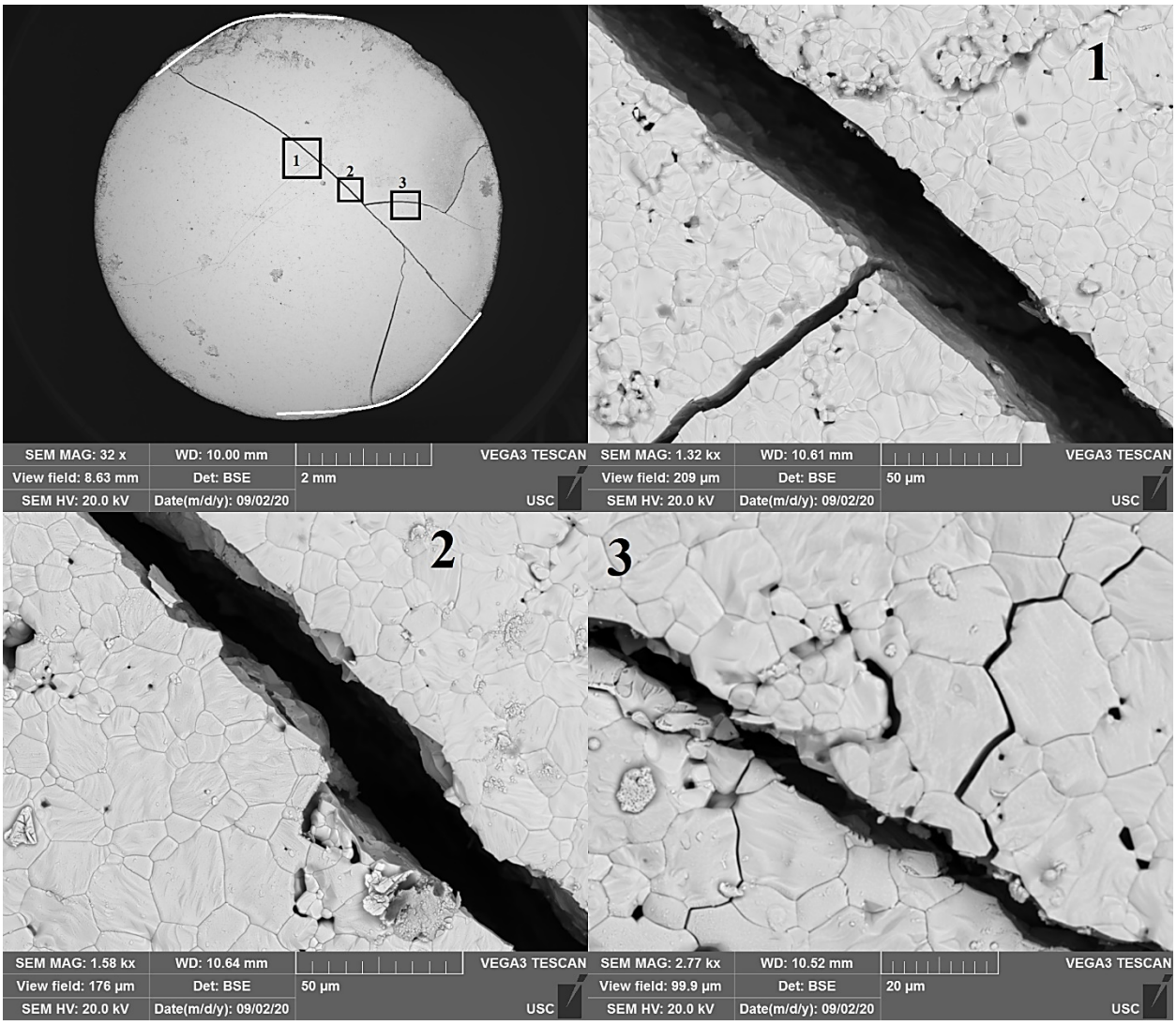

Figure 15. SEM imaging of UO_2 pellet U4-50 (4.0 A) after the resistive heating experiment

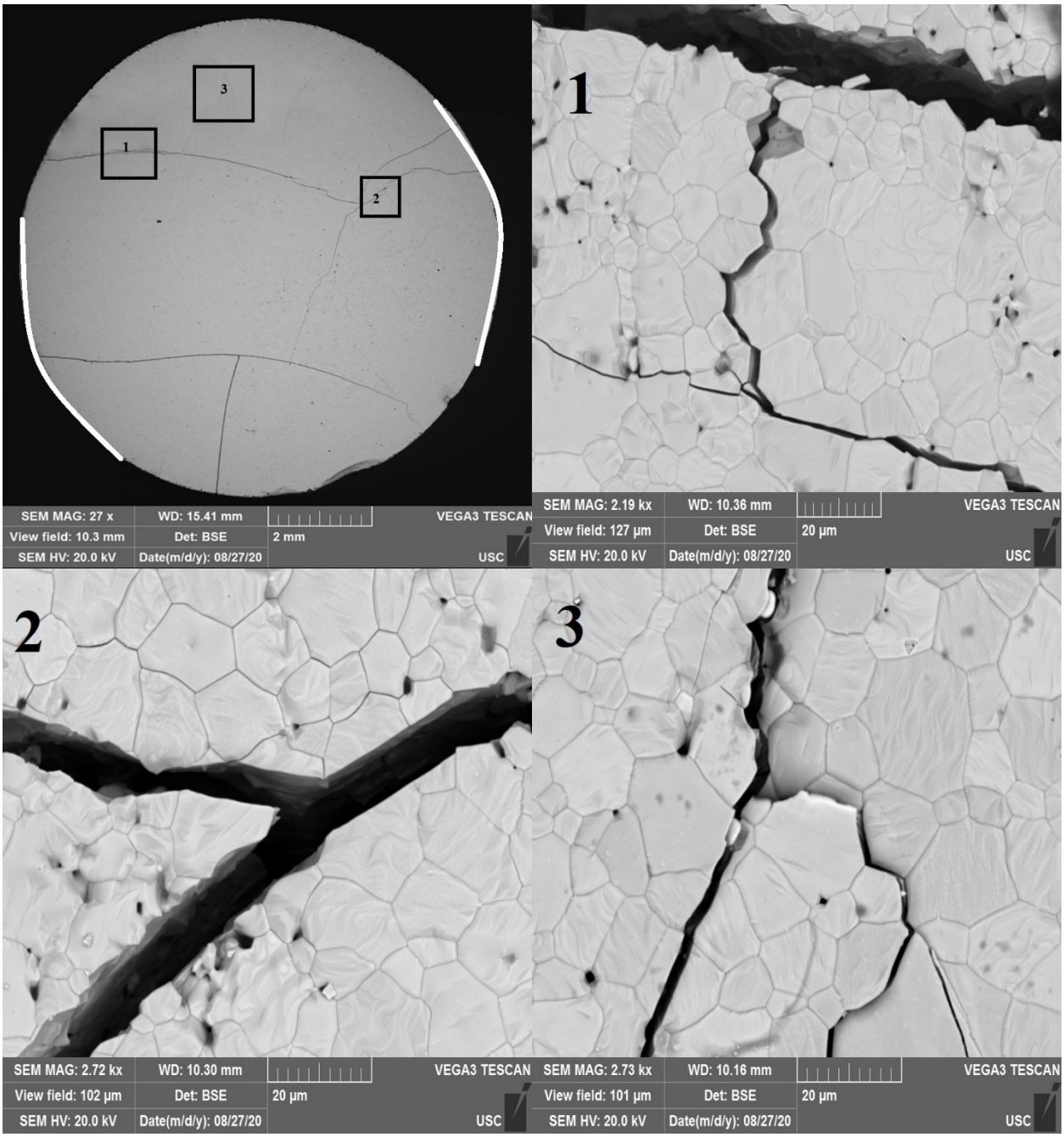

Figure 16. SEM imaging of UO_2 pellet U5-26F (6.0 A) after the resistive heating experiment

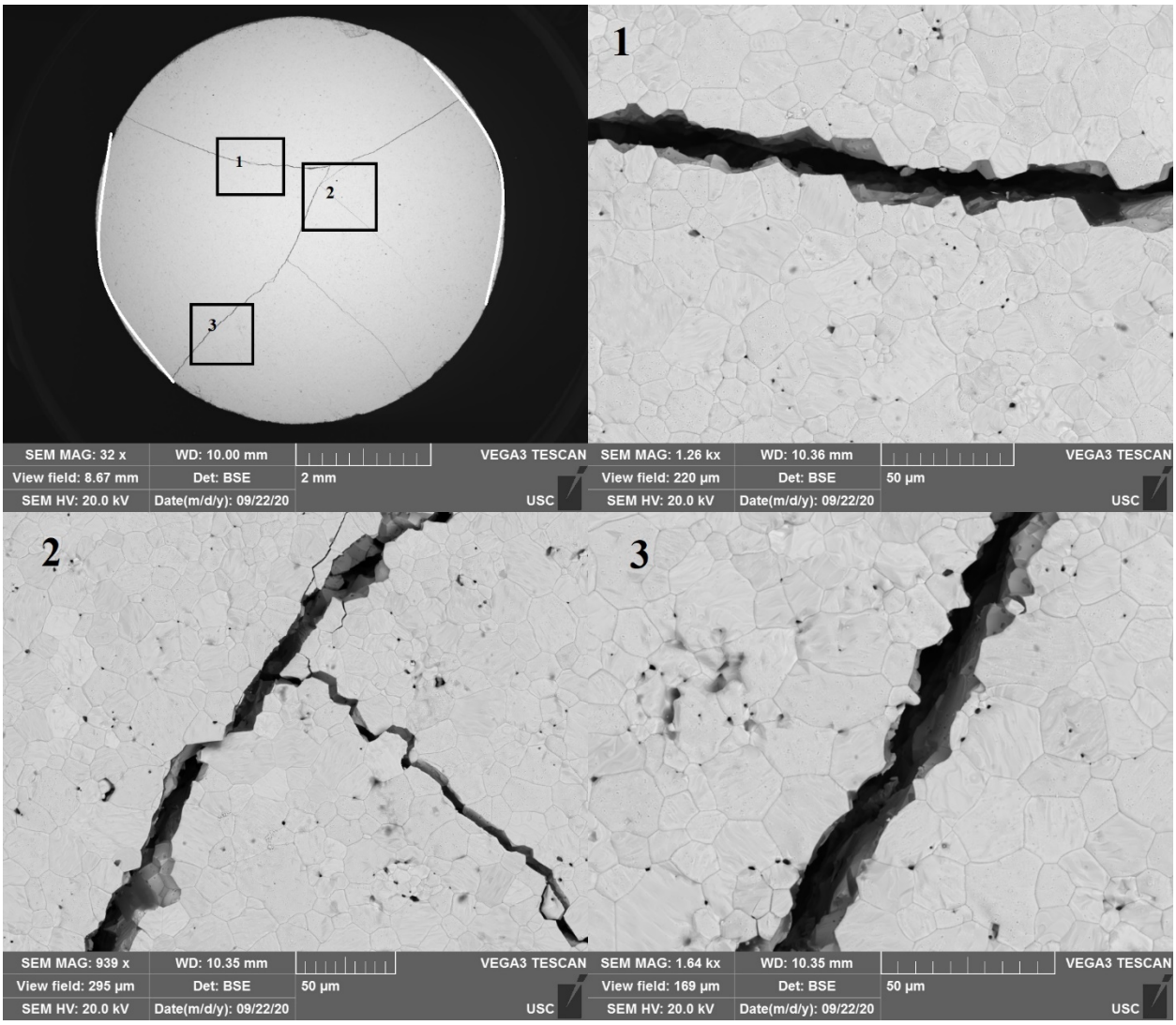

Figure 17. SEM imaging of UO_2 pellet U5-20C (8.0 A) after the resistive heating experiment

It was observed in all the SEMs in Figures 15, 16 and 17 the top left image showing the full face of the pellet reveals that the major primary surface cracks were formed across the diameter of the pellet, generally along the axis between the electrodes. It is difficult to determine whether a single radial crack propagated across the pellet, or whether two radial cracks that formed on opposite sides of the pellet joined in the middle. Regardless, this indicates that the thermally driven hoop stresses were larger near the electrodes than on other portions of the pellet periphery.

The bigger primary surface cracks such as images 1 and 2 in Figures 15, 16 and 17 appear to be very energetic and are a combination of both inter and intra-granular cracking. The primary cracks were highly symmetrical representing cracking patterns quite typical of brittle materials. On the other hand, secondary surface cracks, for example image 3 in Figures 15 and 16 seem to be less energetic and are mostly inter-granular cracking along the grain boundaries. They were likely to be formed at later stages in the cracking process. SEM images 1 and 3 in Figures 15 and 16 show the opening at the sites of primary cracks to be larger than that of the secondary cracks. The primary cracks create stress concentration points that ultimately result in additional cracking. The secondary cracks appear to have branched out from the primary cracks as finer, smaller cracks propagating mostly along the grain boundaries. The large primary cracks in Figures 15, 16 and 17 make it evident that macroscale deformation is entirely due to cracking and not due to inelastic deformation. This is expected due to the short duration of the tests.

Fractography is used here to study the shape of the fractured surfaces. SEM images of fractured surfaces for two different pellets are shown in Figure 18.

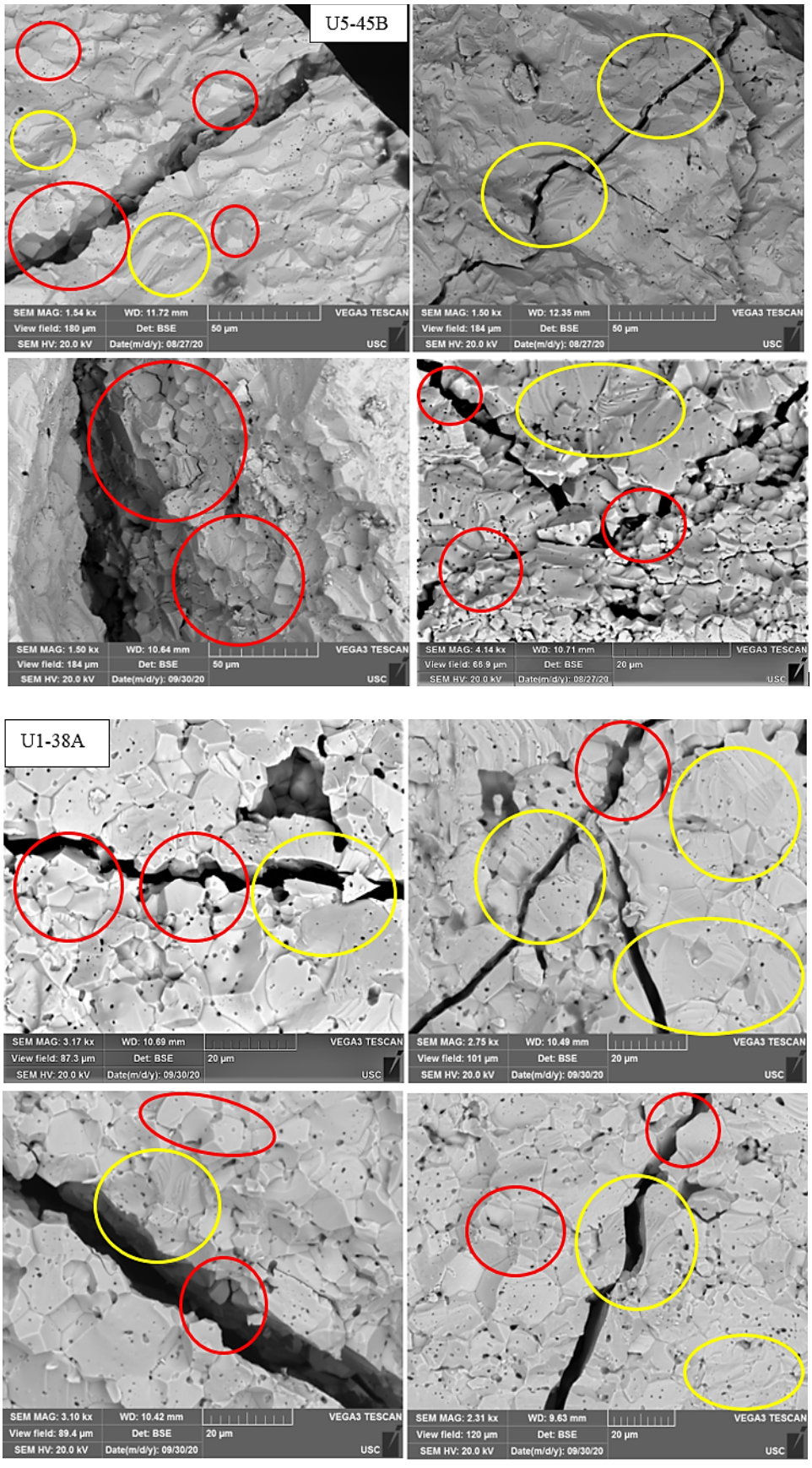
U5-45B
SEM MAG: 1.54 kx
WD: 11.72 mm
VEGA3 TESCAN
View field: 180 µm
Det: BSE
50 µm
SEM HV: 20.0 kV
Date(m/d/y): 08/27/20
USC
SEM MAG: 1.50 kx
WD: 12.35 mm
VEGA3 TESCAN
View field: 184 µm
Det: BSE
50 µm
SEM HV: 20.0 kV
Date(m/d/y): 08/27/20
USC
SEM MAG: 1.50 kx
WD: 10.64 mm
VEGA3 TESCAN
View field: 184 µm
Det: BSE
50 µm
SEM HV: 20.0 kV
Date(m/d/y): 09/30/20
USC
SEM MAG: 4.14 kx
WD: 10.71 mm
VEGA3 TESCAN
View field: 68.9 µm
Det: BSE
20 µm
SEM HV: 20.0 kV
Date(m/d/y): 08/27/20
USC
U1-38A
SEM MAG: 3.17 kx
WD: 10.69 mm
VEGA3 TESCAN
View field: 87.3 µm
Det: BSE
20 µm
SEM HV: 20.0 kV
Date(m/d/y): 09/30/20
USC
SEM MAG: 2.75 kx
WD: 10.49 mm
VEGA3 TESCAN
View field: 101 µm
Det: BSE
20 µm
SEM HV: 20.0 kV
Date(m/d/y): 09/30/20
USC
SEM MAG: 3.10 kx
WD: 10.42 mm
VEGA3 TESCAN
View field: 89.4 µm
Det: BSE
20 µm
SEM HV: 20.0 kV
Date(m/d/y): 09/30/20
USC
SEM MAG: 2.31 kx
WD: 9.63 mm
VEGA3 TESCAN
View field: 120 µm
Det: BSE
20 µm
SEM HV: 20.0 kV
Date(m/d/y): 09/30/20
USC

Figure 18. SEM images showing the fractured surfaces of pellets U5-45B (4.0 A) and U1-38A (5.0 A), both of which underwent resistive heating. Red circled regions indicate intergranular fracture, while yellow circled regions indicate intragranular fracture.

The red circles in the fractographs in Figure 18 show faceted features resembling smooth, rounded, protruded surfaces, signifying the regions of grain boundaries. In these areas, cracks tend to propagate easily along the grain boundaries, since it is thermodynamically easier for cracks to propagate along pre-defined surfaces. In fractography, cracks with obtrusive faces projecting out from the surface mark cracking along the grain boundaries.

On the other hand, the yellow circles highlight the flatter features with band-like structures which mark the intragranular nature of the cracking. Intra-granular cracks grow through the grains. They resemble cracking which follow smooth symmetrical straight-line paths that cleaves the grain itself (see the yellow circles). In the case of intra-granular cracking, the cracks must be highly energetic to create surfaces in the grains themselves to propagate through them when grain boundaries are unavailable. Although some of both types of fracture is observed, the fractured surface analysis reveals the majority of cracking in the fractured surfaces are inter-granular or grain boundary cracking.

6.2. Electrical resistivity measurement

Since the volumetric heating that occurs during resistive heating of UO_2 is highly dependent on electrical resistivity, it is important to characterize the electrical resistivity of the actual UO_2 pellets studied herein. Samples were examined at ambient room temperature using the four-point probe method. A Cascade Microtech C4S-47/0O four-point probe tip was used in conjunction with a Gamry Interface 1010E potentiostat. The four-point probe tip was made from tungsten carbide, has inner probe spacing of 1 mm, and requires a loaded weight of 70–180 g. A fixture was built

for the four-point probe tip and connected to a sample holder (see Figure 19) [26]. The sample holder featured an adjustable height stand to accommodate samples of various heights. The probe tip was fixed to a polycarbonate beam, allowing for additional weight during testing. This type of arrangement ensures that the probe tip and sample remain perfectly leveled during testing. The UO_2 samples were mounted in a nonconductive epoxy and polished prior to resistivity measurements. Calibration was achieved using an undoped intrinsic single-crystal silicon wafer (10 x 10 mm, 100-μm thick) from University Wafer, Inc., with a quoted resistivity of >3000 ohm-cm.

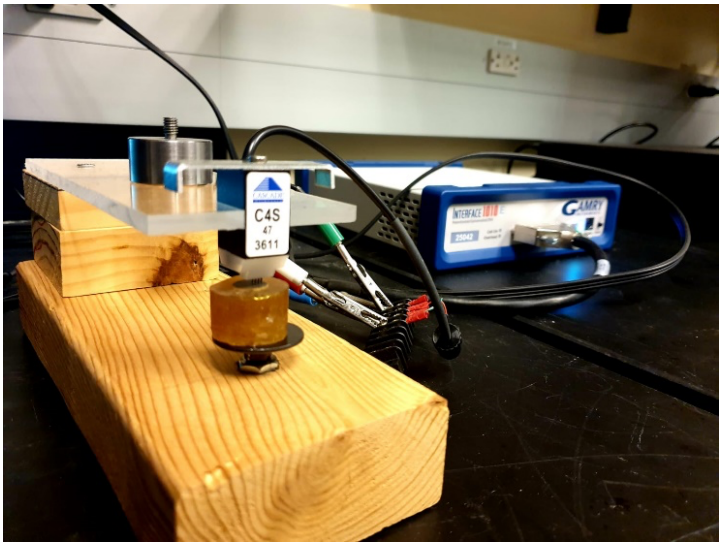

Figure 19. Setup for electrical resistivity measurements of UO_2 pellets at room temperature

The electrical resistivity of two UO2 samples from the same batch of pellets that was subjected to resistive heating testing was measured at room temperature and compared against the study conducted by Bates et al. [15]. For all tests, a total of 180 g in weight was added to top of the probe. This helped maintain proper contact between the probe tips and the sample surface. For an infinitely thin sheet (i.e., a sheet whose thickness is much less than the probe spacing), the sheet's

electrical resistivity is related to its thickness (t), measured voltage (V) and applied current (I) as per the following equation:

$$\rho = \frac{\pi}{ln2} . t . \frac{V}{I}$$

Chronoamperometry analysis was performed by using the Gamry potentiostat, applying a constant voltage of 10 V, and measuring the resultant currents. Each test was performed for 30 s. The two samples' current values are tabulated in Table 4.

Table 4. Current across surfaces of the samples

	Current (amperes); each test averaged 30 s	
Test No.	**Pellet U5-26D**	**Pellet U4-53D**
1	5.30E-06	3.07E-06
2	3.39E-06	5.13E-06
3	7.84E-06	4.01E-06
4	7.12E-06	2.03E-06
5	7.88E-06	4.00E-06
Average	6.31E-06	3.65E-06

Using the results from Table 3, the electrical resistivity of each sample was calculated. The results are shown in Table 5 and graphically compared with each other and with the values indicated by Bates et al [15]. for the same temperature in Figure 20. It is clear that the resistivity is roughly an order of magnitude higher here than that indicated by Bates et al. One likely explanation for this

is that there is a strong observable correlation between resistivity and porosity. Electrical resistivity increases—and conductivity decreases—with increasing porosity in the sample [18]. The UO_2 samples studied by Bates et al. were almost 100% dense, potentially explaining the very high electrical conductivity seen in Figure 20. There is also a direct dependency of the O/U ratio on the electrical conductivity of UO_2. Ishi et al. found that the higher the O/U ratio, the higher the electrical conductivity [27]. However, density and porosity are the primary factors affecting the electrical conductivity of UO_2, not stoichiometry. The pellets investigated here for resistivity measurements have a lower density which explains the significantly higher resistivity values shown in Figure 20.

Table 5. Measured UO_2 electrical resistivity

Sample ID	U5-26D	U4-53D	Bates et al. (1967)
Dimensions (cm)	D = 1.09 H = 0.91	D = 1.10 H = 0.93	D = 0.63 H = 1.9
Fabrication Conditions	1790°C for 24 hours, Ar-5%H2	1790°C for 24 hours, Ar-5%H2	Sintered in commercial grade H2 at 1700C for 12 hours; Heat treated for 8-12 hours at 1125 K in purified Ar-8% H2
Theoretical Density	94.15%	93.4%	100%
Resistance (R ohms)	1.58 X 10^6	2.74 X 10^6	1.38 X 10^6

Resistivity (ρ, ohm-cm) $\rho = \frac{\pi}{ln2} . t . \frac{V}{I}$	2.94 X 10^6	3.94 X 10^6	2.30 X 10^5
Conductivity ($\sigma = 1/\rho$, ohm^{-1} cm^{-1})	3.4 X 10^{-7}	2.54 X 10^{-7}	4.35 X 10^{-6}

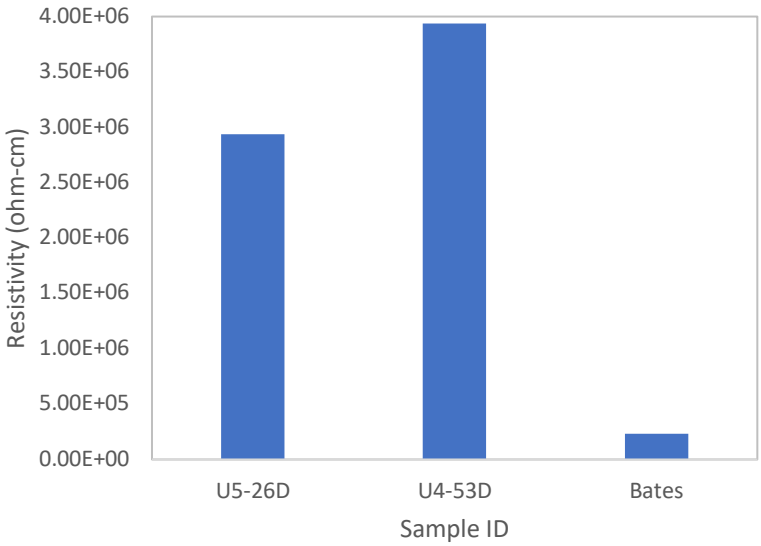

Figure 20. Resistivity of UO_2 samples, as compared to the values in the literature

7. Conclusion

This paper discussed experimental efforts for studying temperature-gradient-driven cracking in UO_2. The three main objectives of this work are: (1) to develop an experimental apparatus that can use resistive heating to replicate the thermal conditions experienced by UO_2 pellets under a variety of operating conditions in the reactor, (2) to collect data using this apparatus for the validation of 2-D and 3-D cracking models in fuel performance codes such as BISON, and (3) to characterize

as-fabricated and cracked pellets to better understand the mechanisms of cracking and explore basic material properties relevant to this study.

It has been demonstrated here that the experimental setup is able replicate the thermal conditions experienced by fresh fuel in an LWR to a reasonable degree. The combined approach of induction and direct resistance heating created volumetric heating within the pellet, which together with radial heat rejection generated temperature profiles in the pellets reasonably close to those expected in the reactor. The thermal gradients produced with this approach led to cracking that is somewhat representative of that which would occur in fresh fuel in the LWR, with a major difference being that the radial cracks in these experiments were largely concentrated on the path between the electrodes in the experiment, while they would be distributed more uniformly around the periphery of fuel in the LWR environment. The direct resistance heating method is flexible in its ability to replicate different reactor power levels rapidly, which allows it to simulate a variety of transient conditions and characterize the accompanying cracking.

The dual imaging system has been shown to be highly useful for characterizing both the thermal conditions and fracture initiation and growth during the experiment, providing data that can be directly used for validation of fracture models in fuel performance codes. Crack formation was visible both through the observed discontinuities in the temperature contours provided by the thermal imaging and the observed cracks in the optical images.

Post-test SEM characterization of cracked and fractured surfaces revealed the formation and propagation of primary cracks along grain boundaries. Measurements of electrical resistivity at room temperature were also taken, providing additional data useful for informing computational models of these experiments.

Acknowledgement

This research is a part of the integrated research project (IRP) IRP FC-1: NEUP Project 16-10905 funded by the U.S. Department of Energy Office of Nuclear Energy's Nuclear Energy University Programs (NEUP) under DE-NE-0008531 funded research project. Fellow graduate students Jonathan McCreary and Jason Reynolds helped in conducting the experiments. The submitted manuscript has been co-authored by a contractor of the U.S. Government under Contract DE-AC07-05ID14517. Accordingly, the U.S. Government retains a non-exclusive, royalty free license to publish or reproduce the published form of this contribution, or allow others to do so, for U.S. Government purposes.

References

1. Oguma, M., CRACKING AND RELOCATION BEHAVIOR OF NUCLEAR FUEL PELLETS DURING RISE TO POWER, Nuclear Engineering and Design, Vol. 76, 1983, pp. 35-45.
2. B. Brzoska, H.P. Fuchs, F. Garzarolli and R. Manzel, Influence of pellet-clad-gap-size on LWR fuel rod performance, Transactions of the 5th SMiRT, D2/1 (1979).
3. D.D. Lanning, The possible impact of fuel pellet cracking on inferred gap conductance and fuel stored energy, Nucl. Technol. 56 (1982) 565.
4. M.P. Bohn, FRACAS--a subcode for the analysis of fuel pellet-cladding mechanical interaction, TREE-NUREG- 1028 (1977).
5. Entropy Limited, SPEAR-BETA Fuel Performance Code System Volume 1. General Description, EPRI NP-2291, Vol. 1, Final Report (1982).
6. K. Ito, M. Ichikawa, T. Nakajima, M. Sogame, T. Okubo and T. Saito, A comparison of FEMAXI-III code calculations with irradiation experiments, Res Mechanica 2 (1981) 109.

7. B. W. Spencer, N. E. Woolstenhume, L. A. Emerson, J.-Y. Yeh, D. D. Imholte, C. M. Hill, D. B. Chapman, C. B. Jensen, M. L. Dunzik-Gougar, T. W. Knight, T. M. Besmann, S. Patnaik, S. M. McDeavitt, L. Ortega, D. Perez- Nunez, and H. Ban. Separate-effects validation experiments for models of fracture in ceramic nuclear fuel. In Proceedings of Top Fuel 2019, Seattle, WA, September 2019.
8. R.L. Williamson, J.D. Hales, S.R. Novascone, G. Pastore, K.A. Gamble, B.W. Spencer, W. Jiang, S.A. Pitts, A. Casagranda, D. Schwen, A.X. Zabriskie, A. Toptan, R.J. Gardner, C. Matthews, W. Liu, and H. Chen. BISON: A flexible code for advanced simulation of the performance of multiple nuclear fuel forms. Nuclear Technology, 2020
9. Yeh, J.Y., Spencer, B. W., Patnaik, S., Knight, T. W., Dunzik-Gougar, M. L., Coupled Physics Simulation of Fracture in Nuclear Fuel Pellets Induced by Resistive Heating, (accepted for publication, Journal of Nuclear Materials, April 2021).
10. Kennedy, C.R., Yaggee, F.L., Voglewede, J.C., Kupperman, D.S., Wrona, B.J., Ellingson, W.A., Johanson, E., Evans, A.G., Cracking and Healing Behavior of UO_2 as Related to Pellet-Cladding Mechanical Interaction. Interim Report prepared for EPRI July 1976. Materials Science Division, October 1976. ANL-76-110.
11. Patnaik, S., Lopes, D.A., Besmann, T.M., Spencer, B.W., Knight, T.W., Experimental System for Studying Temperature Gradient Driven Fracture of Oxide Nuclear Fuel Out of Reactor, Review of Scientific Instruments, DOI: 10.1063/1.5119361, Vol. 91, Issue 3, March 2020.
12. S. Patnaik, D. A. Lopes, B.W. Spencer, T.M. Besmann, E. Roberts, T.W. Knight, Evaluation of Ceria as a Surrogate Material for UO_2 in Experiments on Fuel Cracking Driven by Resistive Heating. (in review)

13. T. M. Besmann, J. W. McMurray, S. Simunovic, “Application of Thermochemical Modeling to Assessment/Evaluation of Nuclear Fuel Behavior,” CALPHAD 55 (2016) 47-51
14. Combat Boron Nitride Solids | Saint-Gobain Boron Nitride; https://www.bn.saint-gobain.com/sites/imdf.bn.com/files/combat-bn-solids-ds.pdf
15. Bates, J.L., Hinman, C.A., Kawada, T., Electrical Conductivity of Uranium Dioxide. Journal of The American Ceramic Society, Vol 50 (12), December 1967, pp. 652-656.
16. Separate Effects Tests for Studying Thermal Gradient Driven Cracking in UO2 pellets Undergoing Resistive Heating, PhD Dissertation, Sobhan Patnaik, University of South Carolina, April 2021.
17. S. Giordano, Electrical behaviour of a single crack in a conductor and exponential laws for conductivity in micro cracked solids, International Journal of Applied Electromagnetics and Mechanics, Vol. 26, 2007, pp. 1–19.
18. Robert K. Willardson, Jerry W. Moody, Harvey L. Goering, The Electrical Properties of Uranium Oxides, Battelle Memorial Inst., Columbus, Ohio, Technical Report, NSA-11-001710, DOE Contract Number: W-7405-ENG-92, 1956.
19. L. Van Brutzel, R. Dingreville, T.J. Bartel, Nuclear fuel deformation phenomena, Chapter 2, NEA/NSC/R(2015)5
20. Olander, D.R. (1976), Fundamental Aspects of Nuclear Reactor Fuel Elements, Technical Report TID-26711-P1, Energy Research and Development Administration, Washington, US.

21. Faya, S.C.S., A Survey on Fuel Pellet Cracking and Healing Phenomena in Reactor Operation. Instituto de Pesquisas Energéticas e Nucleares Sao Paulo – Brasil, INIS, October 1981.
22. Z. Hiezl, Processing and Microstructural Characterization of UO2-based Simulated Spent Nuclear Fuel Ceramics for the UK`s Advanced Gas-cooled Reactors, PhD Thesis, Imperial College of London, 2015.
23. Spino, J., Vennix, K. and Coquerelle, M., Detailed characterization of the rim microstructure in PWR fuels in the burn-up range 40-67 GWd/tM, J. Nucl. Mat. 231, 1996, pp 179-190
24. Kenneth J. Bowles and Richard E. Ghyas, Evaluation of Refractory-Metal-Clad Uranium Nitride and Uranium Dioxide Fuel Pins After Irradiation for Times Up to 10450 hours at 990°C. Lewis Research Center, NASA Technical Note, National Aeronautics and Space Administration, NASA TN 0-7891, June 1975.
25. THERMAL ETCHING PROCESS OF A CERAMIC UNDER OXIDIZING CONDITIONS, Patent NO.: US 6,171,511 B1, Jan. 9, 2001.
26. Metzger, K. E.(2016). Analysis of Pellet Cladding Interaction and Creep Of U3Si2 Fuel For Use In Light Water Reactors. (Doctoral dissertation). Retrieved from https://scholarcommons.sc.edu/etd/3811
27. T. Ishii, K. Naito and K. Oshima, Electrical Conductivity and Defect Structures in Non-Stoichiometric UO_{2+x}, Journal of Nuclear Materials, Vol. 36, 1970, pp. 288-296.